Combustion and Flame 168 (2016) 147–165

Contents lists available at ScienceDirect

Combustion and Flame

journal homepage: www.elsevier.com/locate/combustflame

On periodic behavior of weakly turbulent premixed flame corrugations

Sina Kheirkhah[a,*], Ömer L. Gülder[a], Guillaume Maurice[b], Fabien Halter[b], Iskender Gökalp[b]

[a] University of Toronto, Institute for Aerospace Studies, 4925 Dufferin Street, Toronto, Ontario, Canada
[b] University of Orléans, CNRS ICARE, Avenue de la Recherche Scientifique, Orléans Cedex 2 45072, France

ARTICLE INFO

Article history:
Received 7 August 2015
Revised 9 March 2016
Accepted 9 March 2016

Keywords:
Turbulent premixed combustion
Proper orthogonal decomposition
Symmetric flame fronts
V-shaped flames

ABSTRACT

Periodicity in evolution of premixed methane–air V-shaped flames in the space domain is investigated experimentally. The experiments were performed using the Mie scattering and Particle Image Velocimetry techniques. Three Reynolds numbers of 510, 790, and 1057 along with two fuel–air equivalence ratios of 0.6 and 0.7 were tested in the experiments. The analyses were performed using the Proper Orthogonal Decomposition (POD) technique for the flame front position as well as the velocity data pertaining to non-reacting flow condition. The POD analysis shows that the spectral characteristics of the mode shapes associated with the velocity and the flame front position data feature similarities; however, the corresponding temporal coefficients are significantly different. Specifically, the POD mode shapes pertaining to both velocity and flame front position data feature dominant instabilities. It was shown that the normalized wave number pertaining to these instabilities are similar and equal to the Strouhal number corresponding to non-reacting flow over a circular cylinder. Comparison of the normalized temporal coefficients show that, for the flame front position data, the normalized first and second coefficients are mainly centered close to the origin; however, those associated with the velocity data are positioned around a unity radius circle. This was argued to be linked to the ratio of the corresponding first and second eigenvalues. Specifically, it was shown that, as this ratio approached to unity, the signal energy becomes distributed between the first and the second POD modes. As a result, the normalized temporal coefficients follow a circular pattern.

1. Introduction

Several engineering equipment, for example, stationary gas turbines, lean premixed and pre-vaporized jet engines, and spark ignition engines operate under the mode of turbulent premixed combustion [1–3]. Thus, studying this mode of combustion is of significant importance; and, as a result, numerous laboratory settings have been developed to investigate turbulent premixed flames, see, for example, the review papers [3–5]. These studies show that several flame configurations, e.g., V-shaped, Bunsen-type, swirl-stabilized, spherical, and stagnation, have been utilized to study turbulent premixed flames [3–5]. The flame configuration used in the present study is V-shaped. Previous investigations associated with the V-shaped flames, e.g., [6–8], show that the turbulence intensity (u_{RMS}/U) strongly influences the characteristics of the flame front, where u_{RMS} and U are the root-mean-square (RMS) of velocity fluctuations and the mean velocity in the reactants region, respectively. For relatively small values of the turbulence intensity, i.e., $u_{RMS}/U \lesssim 0.06$, observations reported in Shanbhogue [9], Petersen and Emmons [10], and Kheirkhah and Gülder [8] indicate that the flame front corrugations are periodic and symmetric in the space domain. To the best knowledge of the authors, details associated with these characteristics are yet to be investigated. Since the flame-holder utilized in the present investigation has a circular cross section, a brief review of non-reacting flow development over circular cylinders is presented. Then, findings of past studies associated with the effect of heat release on the flow development are reviewed.

Several investigations have been performed in the past decades to study the development of isothermal flow over circular cylinders, see, for example, the review papers by Berger and Wille [11], Bearman [12], Choi et al. [13], and Williamson [14]. These investigations [11–14] show that the flow development is strongly affected by the Reynolds number estimated based on the diameter of the cylinder (Re_d). For $Re_d \lesssim 5$, the flow is attached to the surface of the cylinder, and the corresponding flow regime is called the creeping flow [15]. For $5 \lesssim Re_d \lesssim 50$, the flow is composed of two steady recirculation zones behind the cylinder, and the pertaining flow regime is referred to as the laminar steady regime [14,15]. Results provided in Zdravkovich [15] show that, for $50 \lesssim Re_d \lesssim 200$,

* Corresponding author.
E-mail address: kheirkhah@utias.utoronto.ca (S. Kheirkhah).

http://dx.doi.org/10.1016/j.combustflame.2016.03.013
0010-2180/

Nomenclature

a_j^i	The jth temporal coefficient for reconstruction of the PIV data associated with the ith image
b_j^i	The jth temporal coefficient for reconstruction of the ith flame front signal
d	Flame-holder diameter
d_p	Seed particle diameter
D	Nozzle inner diameter
$\mathcal{D}$	Mass diffusivity
f_v	Vortex shedding frequency
$\boldsymbol{G}^i$	The ith eigenvector of the flame front data
$\boldsymbol{H}^i$	The ith eigenvector of the velocity data
I	The imaginary unit, $\sqrt{-1}$
K	The total number of data in the velocity field, i.e., 128×128
Ka	The Karlovitz number
l^*	The normalized vertical distance between two local maximums/minimums of the first and the second mode shapes of the velocity data
Le	Lewis number
M	The number of data points associated with the flame front position signal
n	The direction normal to the flame front
N	The number of PIV images, i.e., 1000
$\boldsymbol{p}^i$	The matrix of streamwise and transverse velocity fluctuations associated with the ith PIV image
P	Gas pressure
$\boldsymbol{P}$	The matrix of velocity fluctuations made from $\boldsymbol{p}^i$
Pr	Prandtl number
$\boldsymbol{Q}$	The autocovariance martix of $\boldsymbol{P}$
$r(y)$	the complex function constructed from the flame front position signal and the corresponding Hilbert transform
$\boldsymbol{R}$	The matrix constructed from $\boldsymbol{x}'^i$, $\boldsymbol{R} = [\boldsymbol{x}^1, \boldsymbol{x}^2\ \boldsymbol{x}^3, \ldots, \boldsymbol{x}^N]$
Re_d	The Reynolds number estimated based on the diameter of the flame-holder
$\boldsymbol{S}$	Autocovariance matrix of $\boldsymbol{R}$
S_{L0}	The un-stretched laminar flame speed
St	The Strouhal number
T	Gas temperature
$T_{b,u}$	Burnt and unburnt gas temperature, respectively
$\overline{u}, \overline{v}$	Mean streamwise and transverse velocity, respectively
u', v'	Streamwise and transverse velocity fluctuations
u_{RMS}	RMS of the streamwise velocity fluctuations pertaining to non-reacting flow condition
U	Mean bulk flow velocity
$\vec{V}$	The velocity vector
x, y, z	Axes of the coordinate system shown in Fig. 1(b)
$\overline{x}, x_{RMS}$	Mean and root-mean-square of the flame front position
$x'_{l,r}$	The flame front position fluctuations associated with the left and right wings, respectively
x'^i	The ith matrix of the velocity fluctuations
α	Phase of the flame front position signal
γ^i	The ith eigenvalue associated with the velocity fluctuations
γ_t	The threshold eigenvalue associated with the velocity fluctuations
ϵ	The error associated with estimation of the velocity data
ϵ_i	The inner cut-off length scale
δ_L	Laminar flame thickness
$\boldsymbol{\eta}$	The matrix of the mode shapes utilized for reconstruction of the velocity data
$\boldsymbol{\theta}^i$	The ith normalized POD mode shape associated with the velocity data
κ_c	The critical wavenumber
λ^i	The ith eigenvalue of the flame front position data
Λ	Integral length scale
ν	Gas kinetic viscosity
ρ	Gas density
ρ_u	Unburnt gas density
τ	Time utilized for the statistical analyses $0 \le \tau \le t$
ϕ	Fuel–air equivalence ratio
$\boldsymbol{\psi}^i$	The ith normalized mode shape of the flame front position
$\vec{\omega}$, ω_z	Vorticity vector and the z-component of the vector, respectively

which is known as the laminar vortex shedding regime [14], a global instability develops in the wake of the cylinder. This instability leads to periodic formation and shedding of vortical flow-structures in the wake of the circular cylinder, known as von Kármán vortex street. The vortex shedding frequency (f_v) can be obtained from the following equation [15,16]:

$$St = \frac{f_v d}{U}, \tag{1}$$

where St is referred to as the Strouhal number. For the laminar vortex shedding regime, the Strouhal number increases from approximately 0.12 to 0.19 by increasing the Reynolds number from about 50 to 200 [15,16]. For $200 \lesssim Re_d \lesssim 400$, transition to turbulence occurs in the wake of the cylinder, and the corresponding regime is referred to as the wake transition regime [15]. In this regime, the Strouhal number (St) varies between approximately 0.19 and 0.21. For $400 \lesssim Re_d \lesssim 10^5$, transition to turbulence occurs in the shear layers developed on both sides of the cylinder [15,17]; and the corresponding regime is referred to as the shear layer transition regime [14]. In this regime, the Strouhal number is approximately 0.21. For Reynolds numbers beyond 10^5, the transition to turbulence takes place in the boundary layers developed on both sides of the cylinder, and the corresponding regime is referred to as the boundary layer transition regime [18,19]. The Strouhal number associated with the boundary layer transition regime varies between about 0.2 and 0.5 [15,18,19]. Further details associated with isothermal flow development over circular cylinders can be found in Zdravkovich [15].

Previous studies show that the combustion heat release influences the flow development over circular cylinders [20–26]. This influence can be elaborated using the vorticity transport equation [20], given by:

$$\frac{D\vec{\omega}}{Dt} = (\vec{\omega}\cdot\vec{\nabla})\vec{V} + \nu\nabla^2\vec{\omega} + \frac{\vec{\nabla}\rho\times\vec{\nabla P}}{\rho^2} - \vec{\omega}(\vec{\nabla}\cdot\vec{V}). \tag{2}$$

In Eq. (2), $\vec{\omega}$, $\vec{V}$, ν, ρ, and P refer to vorticity vector, velocity vector, kinematic viscosity, fluid density, and pressure, respectively. The term on the left-hand-side (LHS) of Eq. (2) is the total derivative of the vorticity vector. The first term on the right-hand-side (RHS) is referred to as the vortex stretching and is related to the normal strain in the direction of the vorticity vector. This strain results in narrowing of the vortex tubes, and, as a result, increasing the vorticity values. The second term on the RHS of Eq. (2) is the

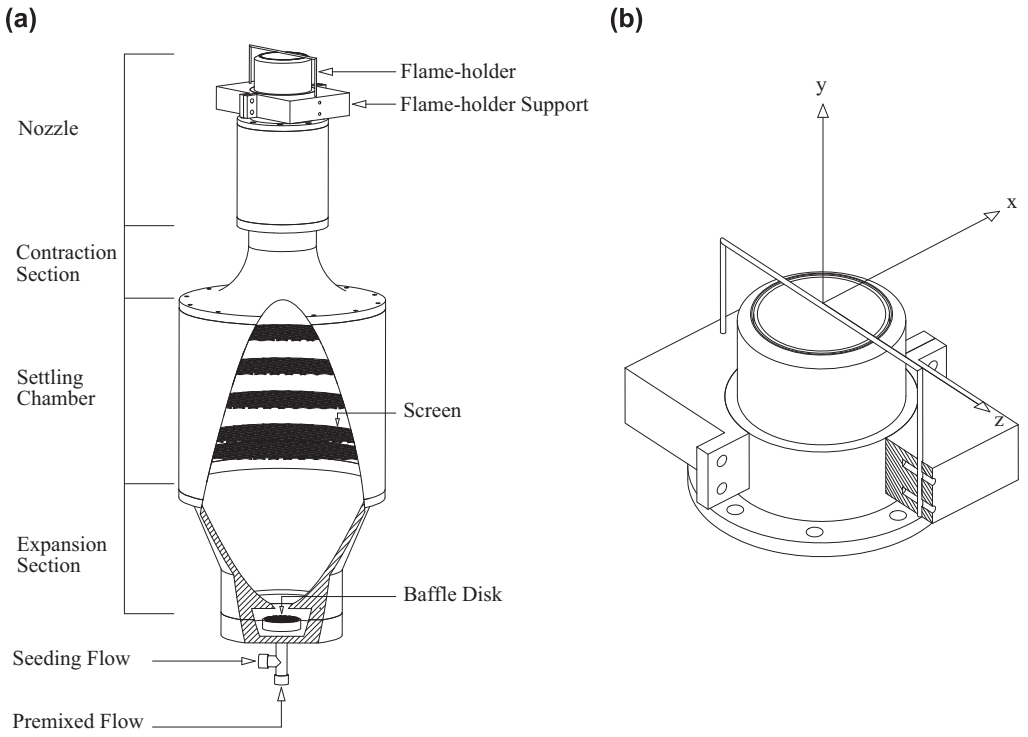

Fig. 1. (a) Burner setup and (b) flame-holder and flame-holder support details.

viscous diffusion term. This term acts as a sink and decreases the vorticity values via the diffusion mechanism [21]. Since the fluid kinematic viscosity increases significantly in the products region, the viscous diffusion term is more pronounced in the products. Thus, the vorticity values decrease significantly across the flame front, from the reactants towards the products. The third term on the RHS of Eq. (2) is produced due to misalignment between the pressure and density gradients. This is a source term and is referred to as the baroclinic vortex generation term [20]. For unconfined flames, which is the case for the present study, the pressure change across the flame region is insignificant; and, as a result, the baroclinic vortex generation is negligible. The last term in the RHS of Eq. (2) is the fluid dilatation term. Due to the significant increase of the velocity through the flame, this term is relatively large.

Arguments provided in past investigations [20,21,27] indicate that, for unconfined flames, the combustion heat release can influence the vorticity equation via the viscous diffusion and the dilatation mechanisms, that are associated with the second and the last terms on the RHS of Eq. (2). Specifically, these mechanisms can affect the formation of the von Kármán vortex street. Results of past investigations associated with formation of the von Kármán vortex street under reacting condition are controversial. Specifically, results presented in Erickson et al. [22] and Hertzberg et al. [24] show that the von Kármán vortex street exists in the wake of the flame-holder; however, results of Yamaguchi et al. [25] and Bill and Tarabanis [26] indicate that it is suppressed under the reacting condition. Arguments provided in Shanbhogue et al. [21] show that either existence or suppression of the vortex street under reacting condition is strongly dependent on the burnt to unburnt gas temperature ratio (T_b/T_u). Specifically, Shanbhogue et al. [21] and Erickson et al. [22] show that strengths of the sink terms in Eq. (2), that are viscous diffusion and dilatation terms, are correlated with T_b/T_u. Their results [21,22] show that, for $T_b/T_u \lesssim 2$, decreasing the burnt to unburnt gas temperature ratio decreases the strengths of the sink terms in Eq. (2), and, as a result, the von Kármán vortex street persists in the wake of the flame-holder. However, for large values of the burnt to unburnt gas temperature ratio ($T_b/T_u \gtrsim 2$), the viscous diffusion and dilatation mechanisms suppress the formation of the von Kármán vortex street. Although past investigations [20–28] provide significant insight into vortex dynamics associated with turbulent premixed flames, detailed description of the connection between characteristics of the flow over the flame-holder and those of the flame fronts are yet to be investigated.

The Proper Orthogonal Decomposition (POD) technique has been extensively utilized in studies pertaining to non-reacting flow over bluff bodies in order to gain insight into the underlying physical processes, see for example, [29–36]. However, to the best knowledge of the authors, application of this technique for analysis of the flame front corrugations is yet to be investigated. This study aims at presenting a detailed description for the POD analysis of the flame front corrugations. Then, using the POD technique, connections between the POD results pertaining to the flame front corrugations and the non-reacting flow over the flame-holder are sought.

2. Experimental methodology

Details of the experimental setup utilized for producing V-shaped flames, the measurements techniques, and the experimental conditions tested are provided in this section.

2.1. Experimental setup

The V-shaped flames were produced using the burner setup presented in Fig. 1(a). The burner is composed of an expansion section, a settling chamber, a contraction section, a nozzle, a flame-holder support, and a flame-holder. The expansion section has an expansion area ratio of about four. Close to the entrance of the expansion section, a baffle disk is placed in order to disperse the entering air–fuel mixture and the seeding flow, see Fig. 1(a). A settling chamber, equipped with five square-mesh screens, is

installed after the expansion section for flow conditioning purposes. The settling chamber is followed by a contraction section with a contraction area ratio of approximately seven. After the contraction section, a nozzle with inner diameter (D) of 48.4 mm is placed. A circular flame-holder, made of stainless steel, is placed close to the exit of the nozzle, see Figs. 1(a) and 1(b). The flame-holder diameter (d) is 2 mm. Using the flame-holder support, the distance between the flame-holder centerline and the exit plane of the burner was fixed at 4 mm during all experiments.

The coordinate system utilized in the present investigation is Cartesian, as shown in Fig. 1(b). The origin of the coordinate system is located equidistant from both ends of the flame-holder, and 5 mm above the burner exit plane. The y-axis of the coordinate system is normal to the exit plane of the burner. The x-axis is normal to both y-axis and the flame-holder centerline. The z-axis is normal to both x and y axes and lies along the span of the flame-holder.

2.2. Measurement techniques

Mie scattering and Particle Image Velocimertry (PIV) techniques were utilized in the present study. The former was used to investigate characteristics of non-reacting flow, and the latter was utilized to study those of the flame front contour. Details pertaining to these techniques are presented below.

2.2.1. Mie scattering

The Mie scattering technique was utilized to obtain the flame front contour. As defined by Eckbreth [37], the Mie scattering is elastic scattering of light, with wave length λ, from particles with average size d_p, when $d_p \gtrsim \lambda$. The Mie scattering technique is widely used in the past experimental investigations pertaining to V-shaped flames, see, for example, [38–45]. An underlying assumption in application of the Mie scattering technique is that combustion occurs inside a relatively thin layer [43–45]. This assumption is referred to as the flamelet assumption [46]. Implication of the flamelet assumption is that if the reactants are seeded with particles which evaporate at the flame front, the light intensities scattered from the particles inside the reactants region will be significantly larger than those inside the products region. This marked difference in the light intensities is utilized for detection of the flame front [42–45]. A Laskin-nozzle type nebulizer, previously utilized in the studies of Smallwood et al. [47], Gülder [48], and Kheirkhah and Gülder [45] was used for seeding purposes in the Mie scattering experiments. The olive oil droplets, which have been previously assessed to be proper for Mie scattering experiments in the past investigations [45,49], were utilized in the present study.

The hardware associated with the Mie scattering technique consists of a CCD camera and a Nd:YAG pulsed laser. The camera has a resolution of 2048 pixels by 2048 pixels. The camera head is equipped with a macro Sigma lens, which has a focal length of 105 mm. During the experiments, the lens aperture size was fixed at f/8. In order to avoid influence of flame chemiluminescence in acquired images, the lens was equipped with a 532 nm band-pass filter. For all the experiments, imaging field of view was 60 mm × 60 mm.

The flow field was illuminated by a laser sheet formed from a 6.5 mm diameter beam, which has a wavelength of 532 nm, a beam energy of about 120 mJ per pulse, and a pulse duration of about 4 ns. At the plane of $z/d = 0$, where all the experiments were performed, the laser sheet thickness was measured to be approximately 150 ± 50 μm. The laser operated at a frequency of 5 Hz and the Mie scattering images were simultaneously acquired by the CCD camera. For statistical analysis purposes, 1000 images were acquired for each experimental condition tested.

The recorded images were binarized using a threshold-based technique. The binarization process is usually accompanied by digitization noise [50]. In order to reduce the noise, a median-finding-based algorithm was utilized to filter the binarized images. The filter size was selected to be equal to the inner cutoff scale (ϵ_i) [50]. The value of the inner cutoff scale was estimated from: $\epsilon_i = 7\delta_L Ka^{-1/2}$ proposed by Roberts et al. [51], where δ_L and Ka are the laminar flame thickness and the Karlovitz number, respectively. Depending on the experimental condition tested, value of ϵ_i was varied between 1.3 mm and 2.5 mm. After filtering the binarized images, the contour algorithm in MATLAB was used to obtain the flame front.

2.2.2. Particle Image Velocimetry

The Particle Image Velocitmetry (PIV) technique was utilized to measure the velocity field for non-reacting flow condition. The PIV experiments were performed for estimating the velocity characteristics pertaining to the background flow field as well as the flow field associated with the wake of the flame-holder. The former was used to estimate the background turbulence intensity as well as the integral length scale (Λ), and the latter was utilized to study the dominant flow-structures. The PIV hardware is identical to that utilized for the Mie scattering experiments. All the PIV experiments were performed at the plane of $z/d = 0$. For each experimental condition tested, 1000 PIV images were acquired at a frequency of 5 Hz. For velocity data analysis, the interrogation window size was selected to be 16 pixels by 16 pixels, with zero overlap between the windows. This results in the velocity data matrices with a size of 128 × 128. For each experimental condition, the separation time between the laser pulses, was selected such that the average distance traced by the seeding particles in each interrogation window was approximately 25% of the size of each interrogation window. This was performed in order to avoid particles loss between consecutive images. Olive oil droplets were used for seeding in the PIV experiments. These droplets were previously assessed [45] to be proper for the flow seeding.

2.3. Experimental conditions

The experimental conditions presented in this study are extracted from a previous investigation by the authors, see [8]. The conditions tested in the present study are associated with relatively small value of the turbulence intensity (u_{RMS}/U). Specifically, u_{RMS}/U is approximately 0.02 and is estimated for the non-reacting flow field, with u_{RMS} being measured at $x/d = 0$, $y/d = -1$, and $z/d = 0$. The tested experimental conditions are tabulated in Table 1. Methane grade 2, i.e., methane with 99% chemical purity, was used as the fuel in the experiments. Three mean bulk flow velocities of U = 4.0, 6.2, and 8.3 m/s were examined. The mean bulk flow velocity was estimated from $U = 4\dot{m}/(\pi \rho_u D^2)$, where $\dot{m}$ and ρ_u are the mass flow rate and density of the fuel–air mixture, respectively. The Reynolds number pertaining to the mean bulk flow velocities were estimated based on the diameter of the flame-holder ($Re_d = Ud/\nu$), with $\nu = 1.57 \times 10^{-5} m^2/s$ being the reactants kinematic viscosity at standard temperature and pressure condition. For each mean bulk flow velocity, two fuel–air equivalence ratios of $\phi = 0.6$ and 0.7 were tested in the experiments. In Table 1, the un-stretched laminar flame speed (S_{L0}) was extracted from Yu et al. [52]. The laminar flame thickness was estimated from: $\delta_L = \mathcal{D}/S_{L0}$, where $\mathcal{D} = \nu/(PrLe)$. The Lewis (Le) and the Prandtl numbers (Pr) are estimated for the reactants mixture at standard temperature and pressure condition; and are approximately unity and 0.71, respectively. For each experimental condition, the integral length scale was estimated using the streamwise velocity autocorrelation [53] calculated along the vertical axis, with

Table 1
Tested experimental conditions.

	Symbol	U (m/s)	Re_d	ϕ	S_{L0} (m/s)	δ_L(mm)	u_{RMS}/U	Λ (mm)
Flame A	○	4.0	510	0.6	0.13	0.17	0.02	2.6
Flame B	□	4.0	510	0.7	0.20	0.11	0.02	2.6
Flame C	◁	6.2	790	0.6	0.13	0.17	0.02	2.5
Flame D	▷	6.2	790	0.7	0.20	0.11	0.02	2.5
Flame E	◇	8.3	1057	0.6	0.13	0.17	0.02	2.4
Flame F	×	8.3	1057	0.7	0.20	0.11	0.02	2.4

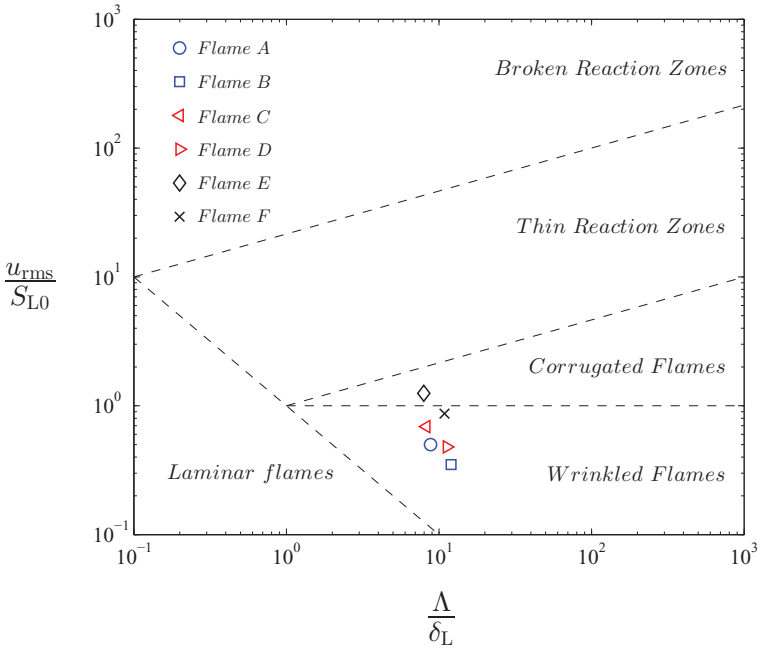

Fig. 2. Experimental conditions overlaid on the premixed combustion regime diagram [1].

details of analysis provided in Kheirkhah and Gülder [8]. All experimental conditions are overlaid on the premixed combustion regime diagram presented in Fig. 2. The results show that the experimental conditions pertain to the wrinkled as well as corrugated flames.

3. Results

A representative Mie scattering image associated with Flame E condition is presented in Fig. 3(a). Overlaid on the figure is the flame front contour obtained from the Mie scattering technique with corresponding details provided in the previous section. Insets of Fig. 3(a) pertaining to the left and right wings of the flame fronts are presented in Figs. 3(b) and 3(c), respectively. Results in the figures show that: (a) the flame front corrugations are symmetric with respect to the vertical axis, and (b) the corrugations feature a nearly periodic pattern. In order to investigate these characteristics, the results are grouped in three subsections. First, details associated with non-reacting flow over the circular cylinder is investigated. Then, in the second and the third subsections, underlying details pertaining to symmetry and periodicity in flame front corrugations are studied, respectively.

3.1. Non-reacting flow characteristics

The POD technique has been utilized for analysis of the results presented in this section as well as those in Section 3.3. This technique has been applied mainly for analysis of non-reacting flow, see, for example, [29–36]. The POD technique can be used for analysis of the processes that are statistically stationary, see for example the results presented in [54,55]. For both non-reacting flow velocity data as well as the fluctuations of the flame front position, it was investigated that the variations of the corresponding parameters are statistically stationary, with the corresponding results presented in Appendix A.

For POD analysis of the non-reacting velocity data, the following matrix was constructed:

$$\boldsymbol{P} = [\boldsymbol{p}^1\ \boldsymbol{p}^2\ \boldsymbol{p}^3\ \ldots\ \boldsymbol{p}^N] = \begin{bmatrix} u_1'^1 & u_1'^2 & u_1'^3 & \ldots & u_1'^N \\ u_2'^1 & u_2'^2 & u_2'^3 & \ldots & u_2'^N \\ u_3'^1 & u_3'^2 & u_3'^3 & \ldots & u_3'^N \\ \vdots & \vdots & \vdots & \vdots & \vdots \\ u_K'^1 & u_K'^2 & u_K'^3 & \ldots & u_K'^N \\ v_1'^1 & v_1'^2 & v_1'^3 & \ldots & v_1'^N \\ v_2'^1 & v_2'^2 & v_2'^3 & \ldots & v_2'^N \\ v_3'^1 & v_3'^2 & v_3'^3 & \ldots & v_3'^N \\ \vdots & \vdots & \vdots & \vdots & \vdots \\ v_K'^1 & v_K'^2 & v_K'^3 & \ldots & v_K'^N \end{bmatrix}, \tag{3}$$

where $\boldsymbol{p}^i = [u_1'^i\ u_2'^i\ u_3'^i\ \ldots\ u_K'^i\ v_1'^i\ v_2'^i\ v_3'^i \ldots\ v_K'^i]^{\rm T}$, with u' and v' being the fluctuations of the streamwise and transverse velocity data.

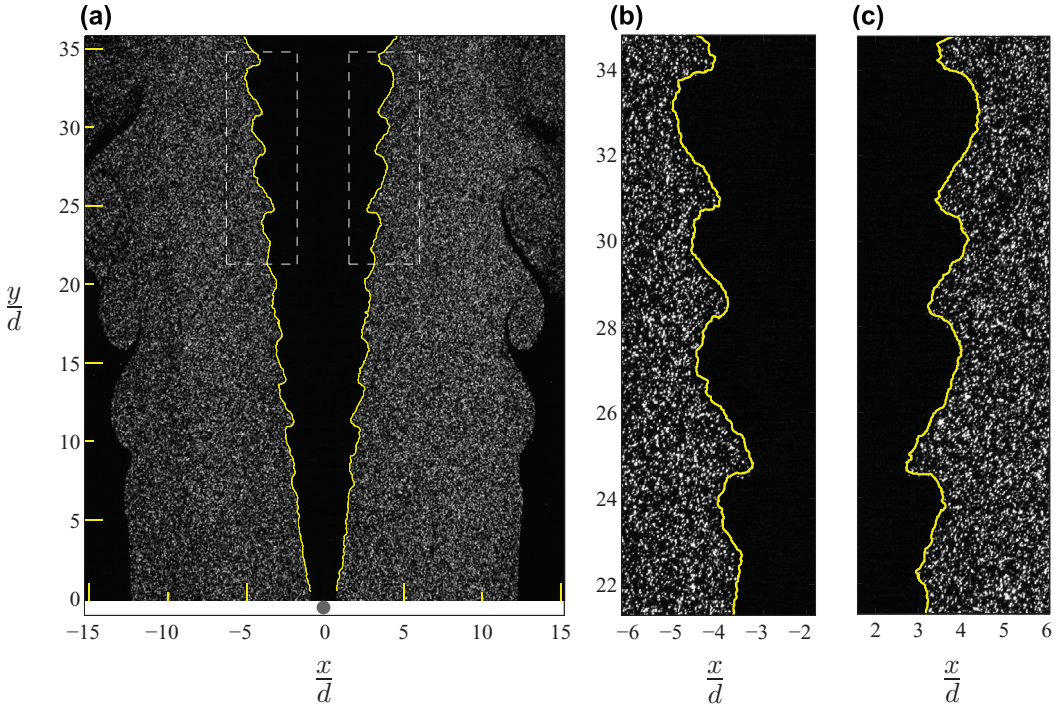

Fig. 3. (a) Mie scattering image associated with Flame E condition. (b) and (c) are insets of (a) pertaining to the left and right wings of the flame fronts, respectively.

Specifically, $u' = u - \overline{u}$ and $v' = v - \overline{v}$, with $\overline{u}$ and $\overline{v}$ being the mean streamwise and transverse velocities, respectively. Each column of $\boldsymbol{P}$ corresponds to velocity fluctuations associated with a given PIV image. Thus, the number of columns in $\boldsymbol{P}$ pertains to the number of PIV images acquired, i.e., $N = 1000$. In Eq. (3), the subscript K is the total number of streamwise or transverse velocity data associated with a given PIV image, meaning that $K = 128 \times 128 = 16384$. Using the matrix of velocity fluctuations, the autocovariance matrix ($\boldsymbol{Q} = \boldsymbol{P}^{\mathrm{T}}\boldsymbol{P}$) was estimated. Then, eigenvalues and eigenvectors of $\boldsymbol{Q}$ were obtained by solving the following equation:

$$\boldsymbol{Q}\boldsymbol{H}^i = \gamma^i \boldsymbol{H}^i, \tag{4}$$

where γ^i and $\boldsymbol{H}^i$ are the ith eigenvalue and eigenvector, respectively. The eigenvalues were estimated and arranged in a descending order, meaning that γ^1 and γ^N correspond to the largest and the smallest eigenvalues, respectively. For all experimental conditions tested, the eigenvalues are presented in Fig. 4(a). Note that, since the analysis is performed for non-reacting flow condition, the results are only presented for experimental conditions of A, C, and E. Results pertaining to experimental conditions of B, D, and F are identical to those pertaining to A, C, and E, respectively. As can be seen from the results in Fig. 4(a), for all experimental conditions tested, the first and the second eigenvalues are relatively large; however, increasing the mode number substantially decreases γ. Since γ^1 and γ^2 are relatively large, the first and the second modes are commonly considered as the most energetic modes in several investigations associated with non-reacting flow over circular cylinders [54,55]. It is usually a necessary practice to estimate the number of meaningful modes associated with the POD analyses. This can be obtained using the uncertainty analysis. In this study, arguments presented in Epps and Techet [56] was utilized to obtain the meaningful number of POD modes. Using uncertainty arguments, Epps and Techet [56] estimated a threshold eigenvalue (γ_{t}) given by the following formulation:

$$\gamma_{\mathrm{t}} = KN\epsilon^2, \tag{5}$$

where ϵ is the error associated with estimation of the velocity data. Assuming negligible bias error, it can be shown that ϵ approximately equals the ratio of the RMS velocity fluctuations to the square root of the number of PIV images. Our analysis shows that the RMS streamwise (u') and transverse (v') velocity fluctuations are maximized in the near wake of the cylinder, with the values of v' being larger. Thus, the maximum value of v' was utilized for estimation of the threshold eigenvalue. The results show that γ_{t} is approximately equal to 3.3×10^4 m^2/s^2, 7.4×10^4 m^2/s^2, and 9.7×10^4 m^2/s^2 for $Re_d = 510$, 790, and 1057, respectively. Results presented in Fig. 4(a) show that eigenvalues associated with modes 1–7, 1–6, and 1–8 are larger than the threshold eigenvalue associated with experimental conditions of A, C, and E, respectively. The corresponding data points are highlighted by the data symbols in Fig. 4(a). The results in the figure suggest that relatively small number of POD modes, approximately first 6 modes, are not contaminated by the velocity data error. Thus, these modes can be utilized for the POD analysis of the velocity data.

The normalized cumulative mode energies ($\sum_{i=1}^{i=n} \gamma^i / \sum_{i=1}^{i=N} \gamma^i$) associated with the results in Fig. 4(a) are presented in Fig. 4(b). The results in Fig. 4(b) show that, for $n \geq 4$, increasing the Reynolds number, decreases the cumulative mode energy. This is associated with pronounced distribution of the turbulent kinetic energy at large mode numbers with increase of the Reynolds number. Specifically, it was previously presented that the background turbulence intensity is approximately constant ($u_{\mathrm{RMS}}/U \approx 0.02$) for all experimental conditions tested, see Table 1. Thus, increasing the Reynolds number, which is synonymous with increasing U, increases the RMS velocity fluctuations associated with the background turbulence (u_{RMS}). On one hand, since the turbulent flow kinetic energy is directly related to u_{RMS}, increasing Re_d increases the kinetic energy of the background turbulent flow. On the other hand, the kinetic energy of the background turbulent flow is distributed amongst large POD modes. Therefore, increasing the Reynolds number distributes the kinetic energy in relatively larger mode numbers. This results in decrease of the cumulative mode energy with increase of the Reynolds number.

Using the eigenvectors estimated from Eq. (4), the normalized POD mode shapes ($\boldsymbol{\theta}^i$) associated with the velocity data were

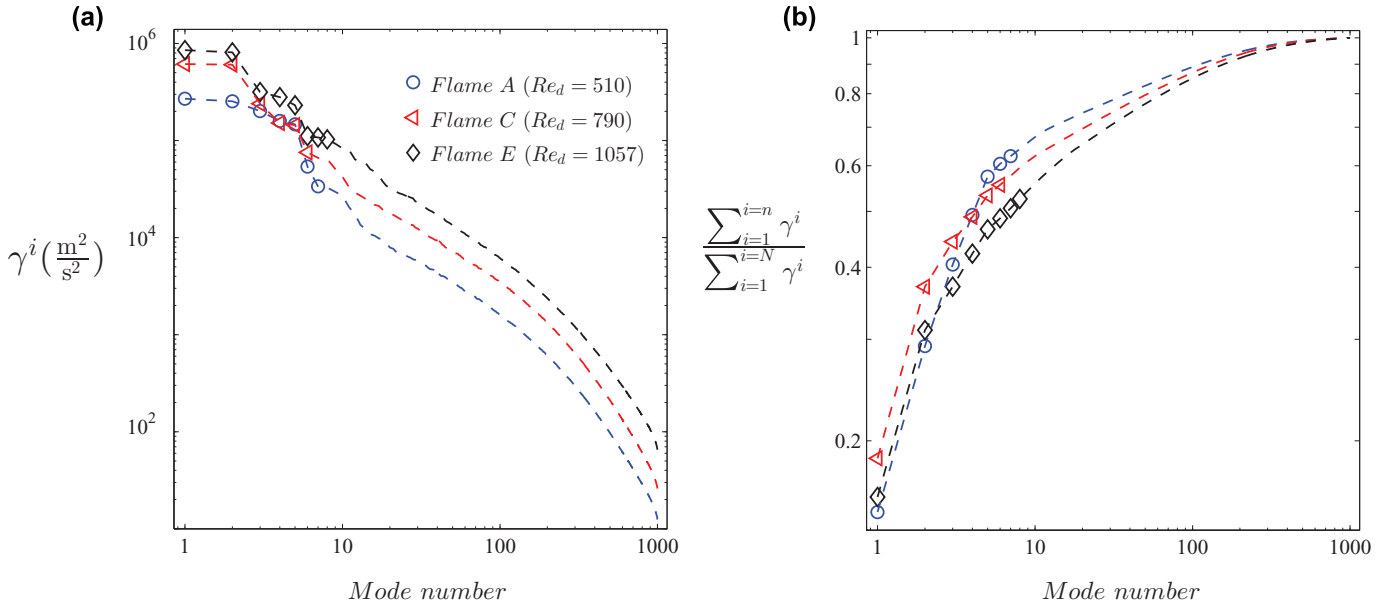

Fig. 4. (a) Eigenvalues of the velocity data. (b) Cumulative mode energy associated with the results presented in (a).

obtained using the following formulation:

$$\boldsymbol{\theta}^i = \frac{\sum_{n=1}^{n=N} h_n^i \boldsymbol{p}^n}{|\sum_{n=1}^{n=N} h_n^i \boldsymbol{p}^n|}, \tag{6}$$

where h_n^i is the nth component of the ith eigenvector. Also, the symbol $(|*|)$ represents the second norm of a matrix. The POD mode shapes estimated from Eq. (6) are matrices with the size of $2K \times 1$. In order to investigate characteristics of the dominant flow-structures, these mode shapes were cast into two dimensional matrices. Specifically, for the ith mode shape, the first and the second K components of $\boldsymbol{\theta}^i$, that are $\boldsymbol{\theta}^i(1:K)$ and $\boldsymbol{\theta}^i(K+1:2K)$, were cast into two 128×128 matrices pertaining to the ith POD mode of the streamwise and transverse velocity data, respectively. It was previously argued that, for the experimental conditions of the present study, mainly modes 1–6 are significant, meaning that these modes are not influenced by the velocity data error. For the analysis presented here and for simplicity of the arguments, only the first ($\boldsymbol{\theta}^1$) and the second ($\boldsymbol{\theta}^2$) POD mode shapes are presented and discussed. Specifically, the first and the second POD mode shapes associated with the streamwise velocity data are presented in Figs. 5(a) and 5(b), respectively. Similarly, the first and the second POD mode shapes pertaining to the transverse velocity data are shown in Figs. 5(c) and 5(d), respectively. In Fig. 5, the negative contours are specified by the overlaid solid curves. The results in Fig. 5 show that the POD mode shapes feature patches of negative and positive values which repeat in the space domain. This is similar to the results presented in past investigations pertaining to flow over circular cylinders, see, for example, Sengupta et al. [57]. Representative variations of the mode shape values associated with Figs. 5(a)–5(d) are presented in Figs. 6(a)–6(d), respectively. The results in Figs. 6(a) and 6(b) are associated with $x/d = 1.5$ and those in Figs. 6(c) and 6(d) pertain to $x/d = 0$. Using the results presented in Fig. 6, the vertical distance between two neighboring local maximums were estimated. This distance normalized by the flame-holder diameter is referred to as l^* and is highlighted in Fig. 6(a). Sensitivity analysis shows that l^* estimated based on the vertical distance between two neighboring local maximums and two local minimums are identical. Also, the results show that l^* is independent of the first and the second POD modes pertaining to either of the streamwise or transverse velocity data, and is approximately 4.2 for all experimental conditions tested. This normalized length scale is considered as the length scale of dominant instability in the wake of the circular cylinder.

It is of interest to investigate the reason associated with the value of l^* being independent of the experimental conditions tested. As it is demonstrated in the following as well as several past investigations pertaining to flow over circular cylinders [14,15], the wake is dominated by the vortex shedding phenomenon for Reynolds numbers similar to those of the present study. Assuming that l is the distance traveled by a given flow-structure in one cycle of vortex shedding, it can be shown that $l = U/f_v$, with f_v being the vortex shedding frequency and is given by Eq. (1). This argument suggests that the Strouhal number, see Eq. (1), and l^* are related by:

$$St \approx \frac{1}{l^*}. \tag{7}$$

Since the Strouhal number is approximately 0.21 for the Reynolds numbers investigated in the present study, see, for example, Zdravkovich [15], l^* requires to be constant, which is in agreement with the results presented earlier. Utilizing the value of Strouhal number along with Eq. (7), it can be shown that l^* is approximately 4.5, which is in reasonable agreement with the results presented in Figs. 5 and 6.

Eq. (7) was derived assuming that l is the vertical distance between two neighboring coherent flow-structures. In order to assess validity of this assumption, the velocity data was reconstructed using the POD modes. This was performed using:

$$\begin{bmatrix} \boldsymbol{u}_r^i \\ \boldsymbol{v}_r^i \end{bmatrix} \approx \begin{bmatrix} \overline{\boldsymbol{u}} \\ \overline{\boldsymbol{v}} \end{bmatrix} + \boldsymbol{\eta}\boldsymbol{\eta}^{\mathrm{T}}\boldsymbol{p}^i, \tag{8}$$

where $\boldsymbol{\eta}$ is associated with the most dominant POD modes and is given by $\boldsymbol{\eta} = [\boldsymbol{\theta}^1\ \boldsymbol{\theta}^2\ \boldsymbol{\theta}^3 \ldots \boldsymbol{\theta}^6]$. In Eq. (8), the superscript i pertains to the data associated with the ith PIV image. In the equation, $\overline{\boldsymbol{u}}$ and $\overline{\boldsymbol{v}}$ are the mean streamwise and transverse velocity data and are given by $\overline{\boldsymbol{u}} = [\overline{u_1}\ \overline{u_2}\ \overline{u_3}\ \ldots\ \overline{u_K}]^{\mathrm{T}}$ and $\overline{\boldsymbol{v}} = [\overline{v_1}\ \overline{v_2}\ \overline{v_3}\ \ldots\ \overline{v_K}]^{\mathrm{T}}$, respectively. Equation (8) can be written in terms of temporal POD coefficients and the dominant POD mode shapes. Specifically, the reconstructed streamwise and transverse velocity data can be given

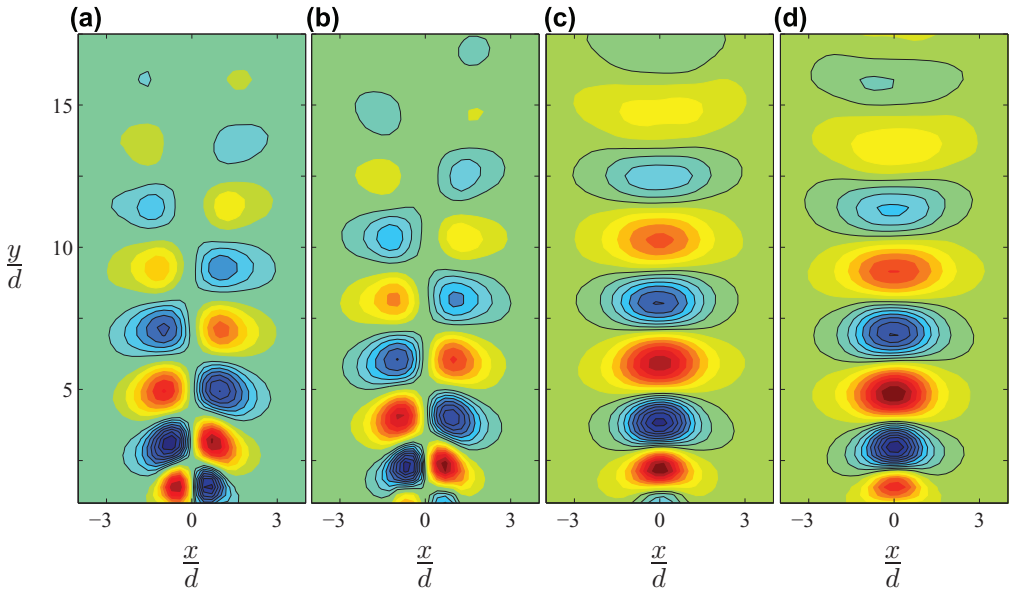

Fig. 5. (a) and (b) correspond to the first and the second POD modes of the streamwise velocity data, respectively. (c) and (d) pertain to the first and the second POD modes of the transverse velocity data, respectively. The results are associated with Flame E condition.

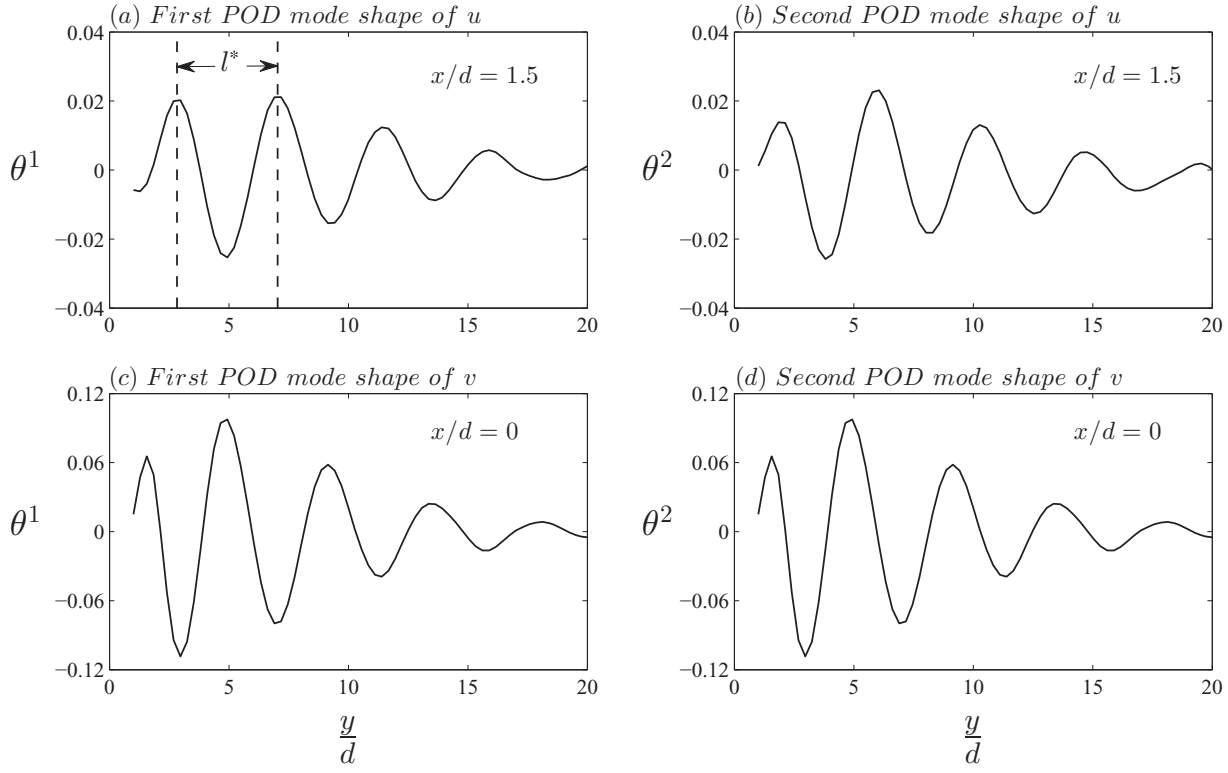

Fig. 6. (a) and (b) are variations of the first and the second POD mode shapes associated with the streamwise velocity data, respectively. (c) and (d) are variations of the first and second POD mode shapes pertaining to the transverse velocity data, respectively. Results in (a, b) as well as (c, d) are associated with $x/d = 1.5$ and 0, respectively. All variations are extracted from corresponding results presented in Fig. 5.

by:

$$\begin{bmatrix} \boldsymbol{u}_r^i \\ \boldsymbol{v}_r^i \end{bmatrix} \approx \begin{bmatrix} \overline{\boldsymbol{u}} \\ \overline{\boldsymbol{v}} \end{bmatrix} + \sum_{j=1}^{j=6} a_j^i \boldsymbol{\theta}^j, \tag{9}$$

where a_j^i is referred to as the jth temporal coefficient for reconstruction of the velocity data associated with the ith PIV image. Figure 7(a) shows a representative vorticity ($\omega_z = \partial u/\partial x - \partial v/\partial y$) contour associated with Flame E condition. The negative vorticity contours are highlighted by solid curves for clarity purposes. The results demonstrate formation of the von Kármán vortex street, which is a characteristic of flow over circular cylinders for Reynolds numbers corresponding to those of the present study. In order to estimate distance between two neighboring coherent flow-structures, variations of vorticity along several vertical distances were considered, with representative ones pertaining to $x/d = -0.7$ and 0.7 presented in Fig. 7(b). The results in Fig. 7(a) show that the normalized distance between two neighboring

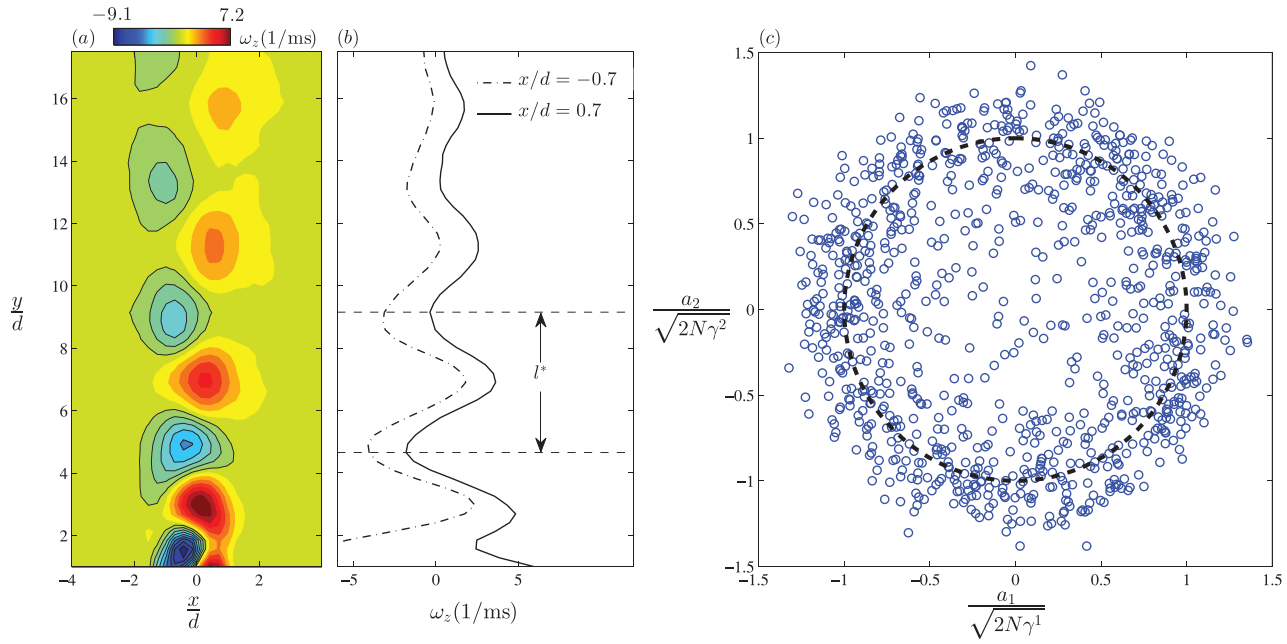

Fig. 7. (a) Representative vorticity contours estimated using the velocity data reconstructed from modes 1–6. (b) Variation of the vorticity presented in (a) along $x/d = -0.7$ and 0.7. (c) Variation of the normalized second POD coefficient versus the normalized first POD coefficient. The results pertain to Flame E condition.

vortices is equal to approximately 4.2. This is identical to the normalized distance previously presented in Fig. 6(a). This similarity validates the assumption that the separation distance between two neigboring coherent flow-structures in the streamwise direction is approximately equal to l.

The vorticity contours presented in Fig. 7(a) demonstrate formation of the von Kármán vortex street. This is a non-stationary process and is associated with the alternate shedding of the vortices. As a result, the first and the second POD modes are expected to feature relatively large energy and length scales (see Figs. 4–6). In addition to this, the first and the second POD modes are temporarily out-of-phase. In order to further asses this, correlation between the first (a^1) and the second (a^2) temporal coefficients were investigated. For the experimental condition associated with the results presented in Fig. 7(a), the normalized temporal coefficients were estimated and the results are presented in Fig. 7(c). As can be seen from the results in Fig. 7(c), the normalized coefficients nearly follow a unity radius circle centered at the origin. This is in agreement with past investigations associated with flow over bluff bodies [58–60]. Further details pertaining to this characteristic of the first and the second normalized temporal coefficients are discussed later in the manuscript.

3.2. Symmetry of the flame front corrugations

Results presented in Fig. 3 showed that the right and the left wings of the flame fronts are nearly symmetric with respect to the vertical axis. In order to investigate this characteristic of the flame fronts, variation of the flame front position along the vertical axis, $x(y)$, was utilized. The flame front position is the distance between a given point on the flame front contour and the vertical axis (y). The analyses presented in this section pertain to mean and RMS of the flame front position as well as the phase difference between the flame front positions associated with the right and the left wings of the flame contours. Representative flame front position signals, extracted from Mie scattering images, are shown in Fig. 8(a). The results in the figure pertain to those previously presented in Fig. 3(a). Mean flame front positions pertaining to both wings of the flame front are presented by the red dashed curves in Fig. 8(a). Also, fluctuations of the left (x'_l) and right (x'_r) wings of the flame fronts are presented in Figs. 8(b) and 8(c), respectively. For the results presented in the rest of the manuscript, signal similar to those shown in Fig. 8 were utilized for the analyses.

Mean and RMS of the flame front position were estimated for all tested experimental conditions, and the corresponding results are shown in Figs. 9(a)–9(c) and 9(d)–9(f), respectively. In the figures, the first, the second, and the third columns pertain to mean bulk flow velocities of 4.0, 6.2, and 8.3 m/s, respectively. The maximum uncertainty associated with the results is accommodated by the size of the error bar in the corresponding figure. The results in the figure show that increasing the fuel–air equivalence ratio increases both $\bar{x}$ and x_{RMS}, with this influence becoming less pronounced with increasing the mean bulk flow velocity. This is a characteristic of lean premixed V-shaped flames and is investigated in detail in past investigations, see, for example, Goix et al. [7] and Kheirkhah and Gülder [45].

The results presented in Fig. 9 show that statistics of $x(y)$ is symmetric with respect to the vertical axis; however, this does not necessitate symmetry of the flame fronts. In order to assess this, phase difference ($\Delta\alpha$) between the right and the left wings of the flame front position were estimated using the Hilbert transform technique. The phase of the flame front position (α) is equal to the phase of the complex function $r(y)$ given by:

$$r(y) = x'(y) - H[x'(y)]I, \tag{10}$$

where $I = \sqrt{-1}$, and $x'(y)$ is the fluctuations of the flame front position along the vertical axis, i.e., $x'(y) = x(y) - \bar{x}(y)$. Representative variation of $x'(y)$ associated with the right and the left wings of the flame front position were previously presented in Figs. 8(b) and 8(c), respectively. In Eq. (9), $H[x'(y)]$ is the Hilbert transform of the flame front position, and is given by:

$$H[x'(y)] = \frac{-1}{\pi y} * x'(y), \tag{11}$$

where the symbol $*$ is the convolution product. For further details associated with the Hilbert transform technique refer to Bracewell [61].

The phase of the right (α_r) and the left (α_l) wings of the flame front were estimated using Eqs. (10) and (11). Variations

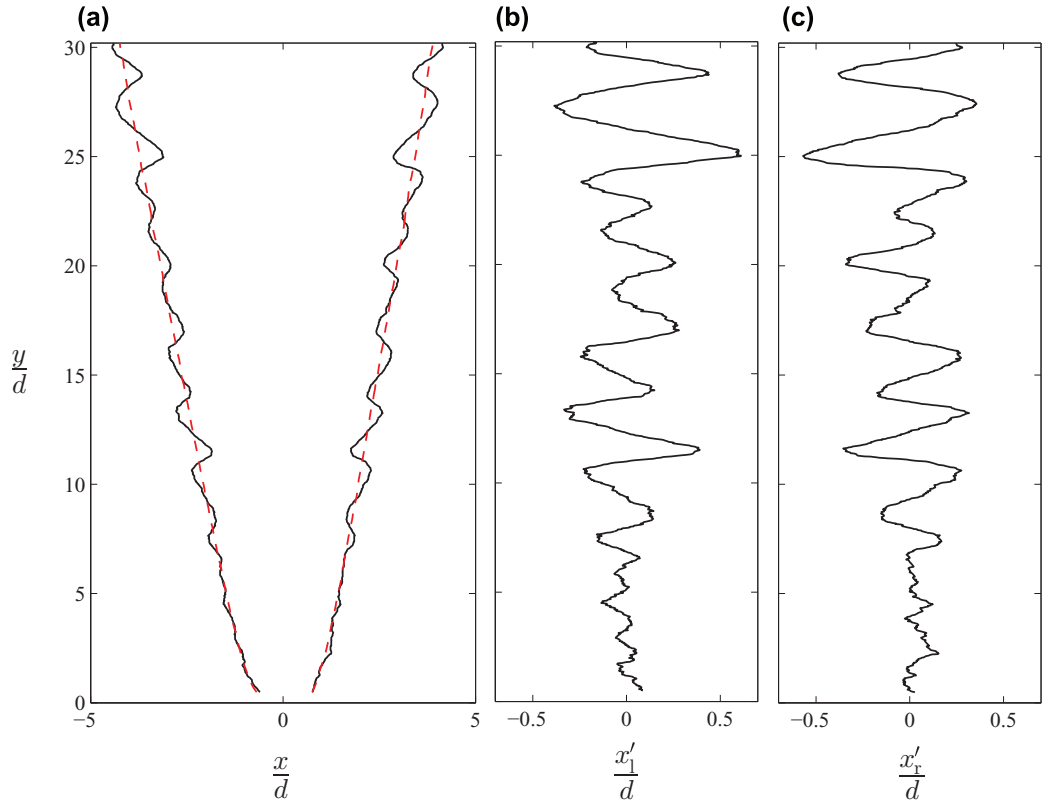

Fig. 8. (a) instantaneous flame front position associated with the results presented in in Fig. 3(a). The red dashed line pertains to the mean flame front position. (b) and (c) are fluctuations of the left and right flame front position along the vertical axis, respectively.

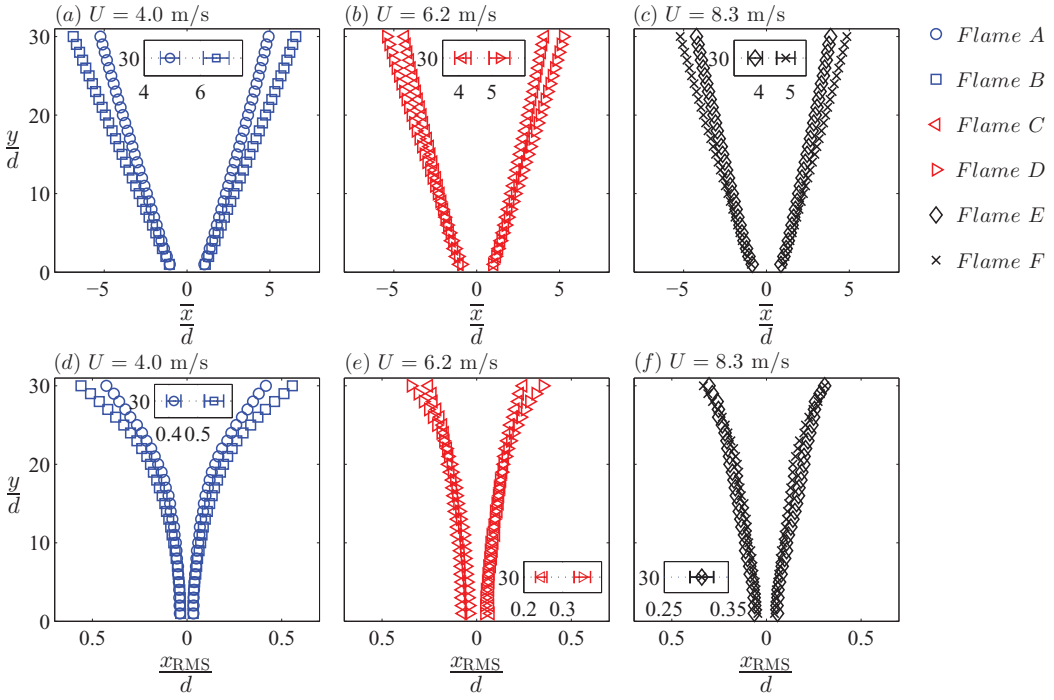

Fig. 9. (a–c) and (d–f) pertain to mean and RMS of the flame front position, respectively. The first, the second, and the third columns pertain to mean bulk flow velocities of 4.0, 6.2, and 8.3 m/s, respectively.

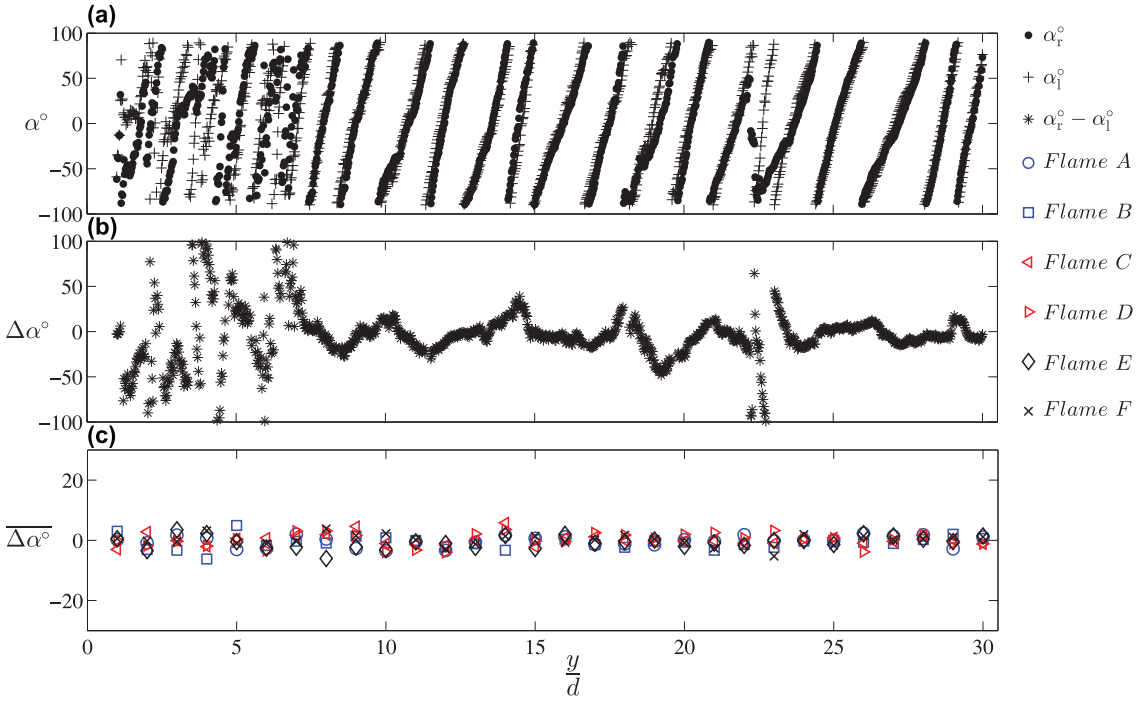

Fig. 10. (a) Instantaneous phase angles associated with the right (α_r) and the left (α_l) wings of the flame front presented in Fig. 3(a). (b) the phase difference pertaining to the results presented in (a). (c) mean of the phase difference for all experimental conditions tested.

of the phase angles associated with the right and the left wings of the flame front are presented in Fig. 10(a). The corresponding phase difference ($\Delta\alpha = \alpha_r - \alpha_l$) is shown in Fig. 10(b). The results in Fig. 10(a) pertain to the flame front fluctuations presented in Figs. 8(b) and 8(c). The results in Fig. 10(a) show that variation of the phase angle along the vertical distance from the flame-holder features a sawtooth shape variation, which is more pronounced at relatively large values of y/d. This characteristic suggests that the flame front corrugations are nearly periodic in the space domain, with further details presented in the next subsection. The results in Figs. 10(a) and 10(b) show that, for relatively small vertical distances from the flame-holder ($y/d \lesssim 8$), α_r and α_l differ significantly; and, as a result, the phase difference is scattered. However, for relatively large vertical distances from the flame-holder, α_r and α_l nearly collapse. Thus, the phase difference is relatively negligible for $y/d \gtrsim 8$, except at $y/d \approx 22$. In fact, for this normalized vertical distance, results in Fig. 10(b) show that $\alpha_r - \alpha_l$ is not negligible. The relatively large values of the phase difference at $y/d \approx 22$ is due to relatively small flame front fluctuations, which leads to error in estimation of the corresponding Hilbert transform.

For all experimental conditions tested, values of the mean phase difference between the right and the left wings of the flame front ($\overline{\Delta\alpha}$) were estimated, with the corresponding results presented in Fig. 10(c). The results in Fig. 10(c) show that $\overline{\Delta\alpha}$ is nearly zero for several vertical distance from the flame-holder and for all experimental conditions tested. This suggests that, on an averaged basis, flame surfaces are symmetrically positioned with respect to the vertical axis.

It is of interest to investigate the underlying reason associated with the symmetry in corrugations of the flame surfaces. Past experimental investigations, e.g., Shanbhogue et al. [9,62], show that, for the conditions pertaining to relatively small values of background turbulence intensity which pertain to the experimental conditions tested in the present study, the large eddies are surrounded by flame fronts. For this reason, the symmetric flame fronts observed in the present study are associated with symmetrically-positioned vortices in the domain of investigation.

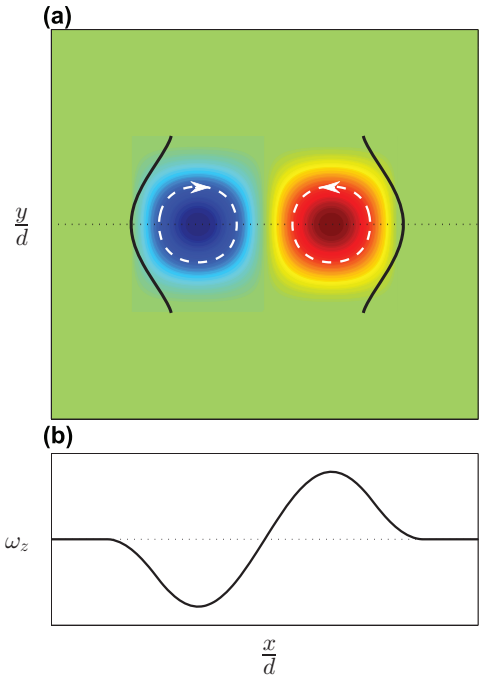

Fig. 11. (a) Schematic interaction of counter-rotating vortices with flame fronts, which are highlighted by black solid curves. (b) Schematic variation of vorticity along the horizontal axis. The variation is presented along the axis passing through the vortices centers, see the dotted line in (a).

Figure 11 presents schematic of two symmetrically-positioned vortices surrounded by flame surfaces which are highlighted by solid black curves. Due to flow and flame front geometries, these vortices require to be counter-rotating. This means that vorticity variation (ω_z) features an odd function at a given vertical distance, with schematic variation presented in Fig. 11(b). In order to prove that the vorticity is an odd function for a given vertical distance, the

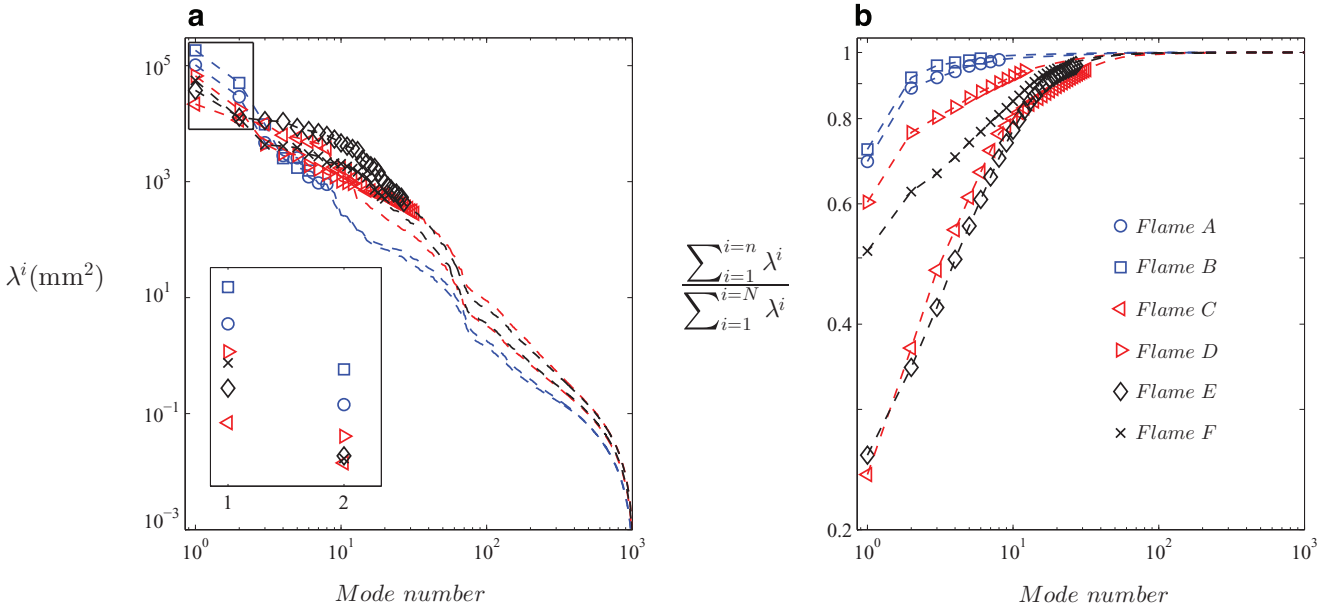

Fig. 12. (a) Variation of the eigenvalue pertaining to flame front position signal. (b) Normalized Cumulative mode energy associated with the results presented in (a).

vorticity transport formulation, Eq. (2), was utilized. Specifically, it was assumed that the flow field is two dimensional, and the vortex stretching as well as baroclinic terms, that are the first and the third terms on the RHS of Eq. (2), are negligible. As a result, Eq. (2) simplifies to:

$$\frac{\partial \omega_z}{\partial t} + v\frac{\partial \omega_z}{\partial x} + u\frac{\partial \omega_z}{\partial y} = \nu\left(\frac{\partial^2 \omega_z}{\partial x^2} + \frac{\partial^2 \omega_z}{\partial y^2}\right) - \omega_z\left(\frac{\partial v}{\partial x} + \frac{\partial u}{\partial y}\right). \tag{12}$$

It can be shown that the vorticity function that satisfies Eq. (12) is an odd function. This means that, for fixed values of t, y, and u, $-v$, $-x$, and $-\omega_z$ satisfy Eq. (12). The ongoing argument suggests that, the heat release causes the viscosity and the dilatation terms on the RHS of both Eqs. (2) and (12) to become dominated. This leads to the vortices to arrange in a symmetric pattern, which causes the symmetry of the flame fronts with respect to the vertical axis.

3.3. Periodicity of the flame front corrugations

The POD technique was utilized to investigate dominant modes of the flame front position signal. The POD technique used in here is similar to that utilized for studying the non-reacting flow characteristics. Specifically, variation of x along the vertical axis is cast into a matrix, given by: $\boldsymbol{x}^i = [x_1^i\ x_2^i\ x_3^i\ \ldots x_M^i]^{\mathrm{T}}$, where the superscript i corresponds to the ith Mie scattering image, and M is the number of data points along the vertical axis, i.e., $M = 1160$. Using $\boldsymbol{x}^i$ along with the mean flame front position ($\bar{\boldsymbol{x}}$), fluctuations of the flame front position signal ($\boldsymbol{x}'^i = \boldsymbol{x}^i - \bar{\boldsymbol{x}}$) were estimated and cast into the following matrix:

$$\boldsymbol{R} = [\boldsymbol{x}'^1\ \boldsymbol{x}'^2\ \boldsymbol{x}'^3\ \ldots\ \boldsymbol{x}'^N] = \begin{bmatrix} x_1'^1 & x_1'^2 & x_1'^3 & \ldots & x_1'^N \\ x_2'^1 & x_2'^2 & x_2'^3 & \ldots & x_2'^N \\ x_3'^1 & x_3'^2 & x_3'^3 & \ldots & x_3'^N \\ \vdots & \vdots & \vdots & \vdots & \vdots \\ x_M'^1 & x_M'^2 & x_M'^3 & \ldots & x_M'^N \end{bmatrix}, \tag{13}$$

where N is the number of acquired Mie scattering images, i.e., $N = 1000$. Using $\boldsymbol{R}$, the autocovariance matrix ($\boldsymbol{S} = \boldsymbol{R}^{\mathrm{T}}\boldsymbol{R}$) was estimated. The eigenvalues (λ^i) and eigenvectors ($\boldsymbol{G}^i = [g_1^i\ g_2^i\ g_3^i\ \ldots\ g_N^i]^{\mathrm{T}}$) of the autocovariance matrix were obtained by solving the following eigenvalue problem:

$$\boldsymbol{S}\boldsymbol{G}^i = \lambda^i \boldsymbol{G}^i. \tag{14}$$

For all experimental conditions tested, the eigenvalues and the corresponding eigenvectors were obtained from Eq. (14). The eigenvalues were arranged in a descending order and are presented in Fig. 12(a), with the corresponding normalized cumulative mode energies presented in Fig. 12(b). Following the arguments presented in Section 3.1., the number of meaningful POD modes, also referred to as the threshold mode number, were estimated for analysis of the flame front corrugations. Specifically, for Flames A, B, C, D, E, and F, the mode numbers pertaining to the threshold eigenvalue are 8, 6, 32, 12, 27, and 20, respectively. In Fig. 12(a), results associated with the mode numbers smaller than those obtained from the threshold eigenvalue are highlighted by the corresponding data symbols. The results pertaining to the eigenvalues of the first two modes (λ^1 andλ^2) are enlarged and shown in the inset of Fig. 12(a). As can be seen from the results in the figure, λ is dependent on the experimental conditions tested. Specifically, for the first mode, the results show that increasing the fuel–air equivalence ratio increases λ. For the second mode, a similar trend is observed, except for $U = 8.3$ the result show that λ is nearly insensitive to the variation of the fuel–air equivalence ratio. Compared to the first and the second modes, for the mode numbers larger than two, increasing ϕ decreases the corresponding eigenvalues. Since the eigenvalues are associated with the energy of the flame front position, RMS of this parameter (x_{RMS}) was utilized to investigate influence of the fuel–air equivalence ratio on the first and the second POD modes. Values of x_{RMS} were previously investigated, and the corresponding results were presented in Figs. 9(d)–9(f). As the results presented in the figure show, x_{RMS} increases along the vertical axis. In order to facilitate comparisons, the maximum value of x_{RMS} was utilized for the arguments. This parameter is approximately 0.9, 1.15, 0.5, 0.7, 0.6, and 0.6 mm, for the right wings of Flames A, B, C, D, E, and F, respectively. Comparison of the results pertaining to the maximum value of x_{RMS} show that for $U = 4$ and 6.2 m/s increasing ϕ increases the maximum value of x_{RMS}; however, this parameter is almost insensitive to the variation of the fuel–air equivalence ratio. This trend is similar to that associated with influence of ϕ on the first and the second mode eigenvalues.

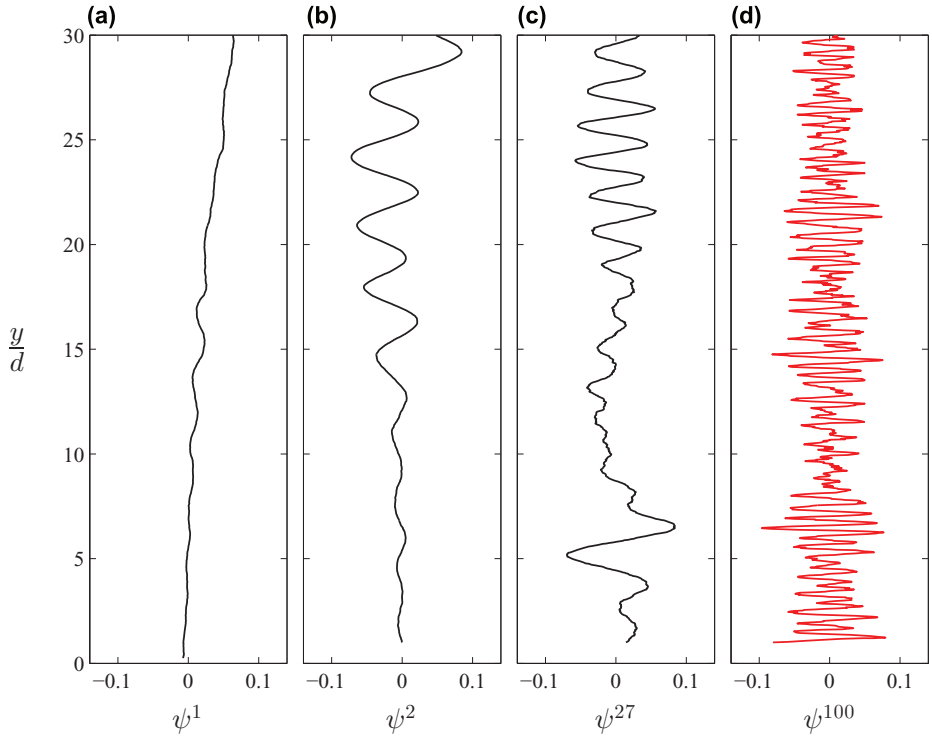

Fig. 13. Mode shapes associated with Flame E condition. (a)–(d) pertain to the first, the second, the twenty seventh, and the one hundredth modes, respectively.

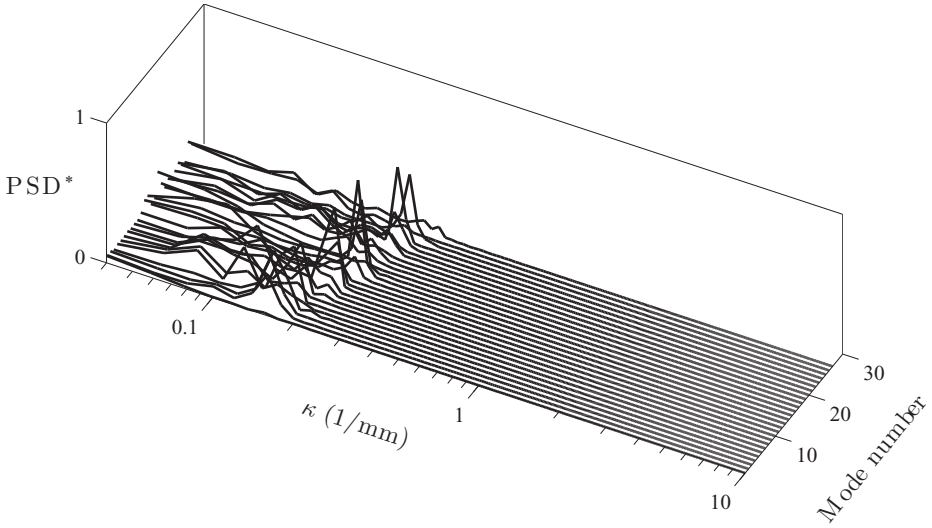

Fig. 14. Normalized power spectrum densities of the mode shapes associated with Flame E condition.

In order to investigate the periodicity of the flame front corrugations, the POD mode shapes were estimated using the following formulation:

$$\boldsymbol{\psi}^i = \frac{\sum_{n=1}^{n=N} g_n^i \boldsymbol{x}'^i}{\left|\sum_{n=1}^{n=N} g_n^i \boldsymbol{x}'^i\right|}. \tag{15}$$

Figures 13(a)–13(d) present the first, second, twenty seventh, and one hundredth POD mode shapes associated with Flame E condition. The POD mode shape pertaining to the largest mode number is dominated by uncertainty in estimation of the flame front position signal, and is highlighted in red. The results in Figs. 13(a)–13(c) show that increasing the mode number increases fluctuations of $\boldsymbol{\psi}$ along the vertical axis. In order to investigate this, normalized power spectrum densities (PSD^*) associated with $\boldsymbol{\psi}^1$ to $\boldsymbol{\psi}^{27}$ were estimated. The values of PSD^* were obtained using the FFT technique. The number of data points utilized for the FFT analysis was selected to be 2^{10}. This leads to a resolution which allows for resolving the dominant wave numbers associated with the corrugations of the flame front, while avoiding noise in the FFT analysis. The results pertaining to the normalized power spectrum densities of the POD mode shapes are presented in Fig. 14. Since the POD mode shapes pertaining to mode numbers larger than 27 are influenced by measurement uncertainty, only results associated with $\boldsymbol{\psi}^1$ to $\boldsymbol{\psi}^{27}$ are presented in the figure. As can be seen, for a given mode number, PSD^* features a dominant peak. The wave number pertaining to the peak, is referred to as κ_c, and features an increasing trend with increasing the POD mode number, which is in agreement with the results presented in Fig. 13.

Values of the dominant wave number (κ_c) pertaining to the results in Fig. 14 are presented in Fig. 15. The uncertainty in

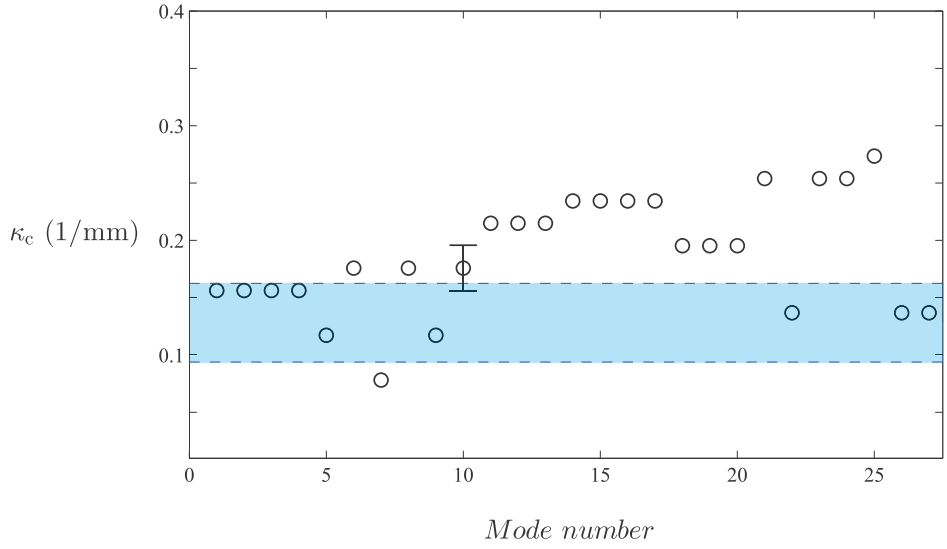

Fig. 15. Variation of the most dominant wave number associated with the results presented in Fig. 14.

estimation of κ_c pertains to the resolution of the spectral analysis and is accommodated by the size of the error bar in the figure. Also shown in the figure is the dominant wave number $(1/l)$ pertaining to the non-reacting flow over a circular cylinder. Value of $1/l$ can change approximately by twice of the PIV measurements resolution. This leads to an error in estimation of $1/l$ which is shown by the highlighted region in Fig. 15. The results in the figure suggest that, for Flame E condition, the dominant wave numbers associated with mode numbers 1–10 of the flame front corrugations match the dominant wave number pertaining to non-reacting flow over a circular cylinder. Similar results were obtained for the rest of the experimental conditions tested. Specifically, it was obtained that, for Flames A, B, C, D, and F, spectral characteristics of the first 8, 6, 8, 10, and 7 modes match those of the non-reacting flow, respectively. This suggests that, for the experimental conditions tested, the length scale associated with the flame front wrinkling is similar to the separating distance between vortices associated with non-reacting flow over a circular cylinder.

Comparison of the results presented in this section with those in the previous section may seem to suggest contradictory conclusions. On one hand, the results in the previous section showed that the flame fronts are symmetric with respect to the vertical axis. As a results, it was concluded that the vortices are arranged differently from those in the von Kármán vortex street, which suggests that the von Kármán instability is not present for the reacting conditions tested in this study. On the other hand, the length scale associated with the flame surfaces and that pertaining to non-reacting flow over a circular cylinder are similar. The authors believe that this similarity does not necessitate formation of the von Kármán vortex street under reacting condition. In fact, past investigations, e.g., Shanbhogue et al. [62] show that origin of the vortices which lead to corrugation of the flame surfaces is linked to the shear layer instability formed on both sides of the flame-holder. The authors believe that, comparison of the results associated with the POD analysis of the flame front corrugations with those pertaining to the velocity data for reacting condition can potentially allow to gain further insight into to the symmetry of the flame front corrugations. However, due to the arguments presented in Appendix B, the velocity measurements associated with reacting condition were not performed in the present investigation.

Using the POD mode shapes, the flame front position signal was reconstructed utilizing the following formulation:

$$\boldsymbol{x}_r^i = \bar{\boldsymbol{x}} + \boldsymbol{\eta}\boldsymbol{\eta}^T \boldsymbol{x}'^i, \tag{16}$$

where $\boldsymbol{x}_r$ is the reconstructed flame front position signal and $\boldsymbol{\eta} = [\boldsymbol{\psi}^1\ \boldsymbol{\psi}^2\ \boldsymbol{\psi}^3\ \ldots \boldsymbol{\psi}^m]$. The number of columns of $\boldsymbol{\eta}$ is the number of POD modes utilized for reconstruction of the flame fronts. For the results presented here, Flame E condition was utilized as this condition was extensively studied in the previous subsections. However, similar results were obtained for the rest of the experimental conditions tested. For reconstruction of the flame fronts, m was set to 5, 10, and 27. The last two values of m were selected as they correspond to the number of modes that can capture spectral characteristics of the flame front as well as the number of modes that are not significantly influenced by uncertainty of measurements, respectively. In addition to these, results associated with $m = 5$ were considered for comparison purposes. The reconstructed flame fronts pertaining to $m = 5$, 10, and 27 are presented by the red dotted, blue dashed, and green dotted-dashed curves in Fig. 16, respectively. The experimentally obtained flame front, which corresponds to the results presented in Fig. 3, is shown by the solid black curve. An inset of Fig. 16(a) is enlarged and shown in Fig. 16(b). Comparison of the results presented in Fig. 16(b) shows that the first 10 and 27 modes can capture fluctuations of the flame front. This is in comparison with the results pertaining to $m = 5$, which show that the corresponding reconstructed flame front does not follow the flame front obtained from the Mie scattering images. The arguments provided above suggest that, for Flame E condition, the set of POD modes, with spectral characteristic similar to that pertaining to non-reacting flow over a circular cylinder, can adequately capture fluctuations of the flame front along the vertical axis. In fact, this is the case for all experimental conditions tested in the present study.

Using the required number of POD modes for reconstruction of the flame fronts, it can be shown that Eq. (16) simplifies to:

$$\boldsymbol{x}_r^i \approx \bar{\boldsymbol{x}} + \sum_{j=1}^{j=10} b_j^i \boldsymbol{\psi}^j, \tag{17}$$

where b_j^i is referred to as the jth temporal coefficient for reconstruction of the ith flame front position signal. In Eq. (17), the upper bound of summation is associated with the maximum number of modes pertaining to Flame E condition. Following the above arguments, the upper bound of summation for Flames A, B, C, D, and F, are 8, 6, 8, 10, and 7, respectively. It was previously argued that spectral characteristics of $\boldsymbol{\psi}^j$ is similar to that of non-reacting

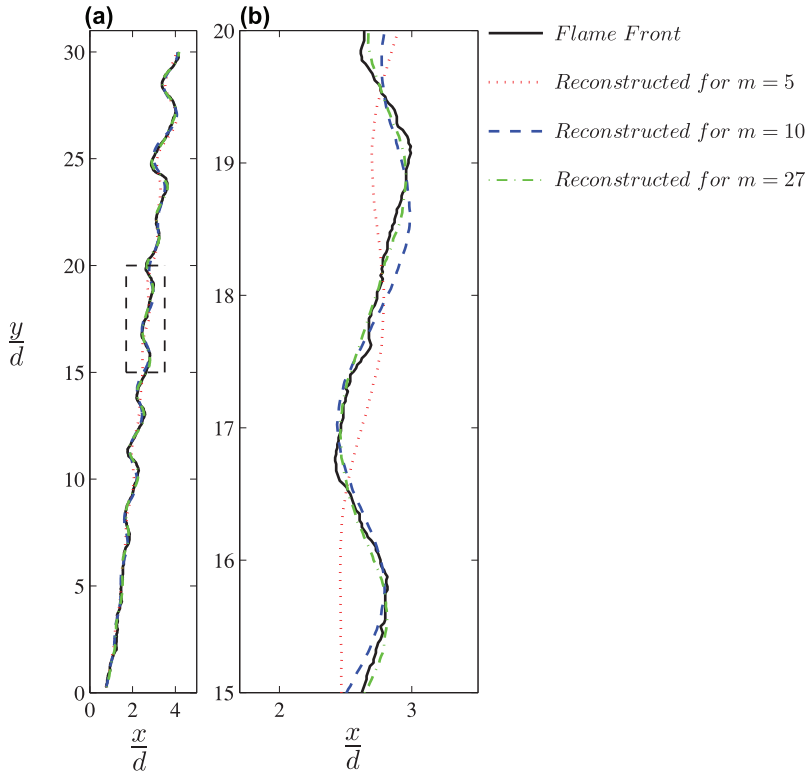

Fig. 16. (a) Reconstruction of the flame front position signal associated with the results presented in Fig. 3(a). (b) is the inset of (a).

flow. It is of interest to compare the characteristics of the first and the second temporal coefficients for the non-reacting flow (a_1 and a_2) with those pertaining to flame front fluctuations (b_1 and b_2). Figure 17(a) shows variation of the normalized temporal coefficients pertaining to the flame front fluctuations for all flame front position signals associated with Flame E condition. As can be seen from the results in the figure, the normalized coefficients are distributed in the plane of $b_1 - b_2$ with most of the data points positioned relatively close to the origin. For flame front position signals with relatively small values of b_1 and b_2, most of the energy is distributed between relatively large number of modes. As a result, fluctuations of the flame front signal along the vertical axis are expected to feature a relatively small wave number. In comparison to the energy of the flame front position signals with relatively small values of b_1 and b_2, energy of those associated with relatively large values of b_1 and/or b_2 is mostly distributed in smaller number of modes. Thus, the corresponding fluctuations of the flame front position signal is expected to feature a relatively smaller wave number. In order to assess this, two representative data points were selected and highlighted in Fig. 17(a). One point is positioned relatively close to the origin, highlighted by the blue solid circular data point; and the other point is positioned relatively far from the origin, highlighted by the red solid circular data point. Fluctuations of the flame front position pertaining to the blue and the red data points are shown by the blue solid and the red dashed curves in Fig. 17(b), respectively. For clarity purposes, the scale of the horizontal axis is selected to be larger than that of the vertical axis. Normalized power spectrum densities associated with the results in Fig. 17(b) are presented in Fig. 17(c). As can be seen from the results in Fig. 17(c), the dominant wave number associated with the solid curve is larger than that pertaining to the dashed curve. This means that the energy of the flame front position associated with the solid curve, in comparison to that pertaining to dashed curve, is distributed in larger mode numbers. Thus, in agreements with the results in Fig. 17(a), the first two POD coefficients associated with the solid curve are positioned closer to the origin in comparison to the coefficients corresponding to the dashed curve.

Comparison of the results presented in Fig. 17(a) with those in Fig. 7(c) shows that the relation between the first and the second temporal coefficients associated with the flame front position and the velocity data do not follow a similar trend. Specifically, results associated with the velocity data showed that the coefficients are positioned around a unity radius circle; however, those associated with the flame front fluctuations are mainly positioned close to the origin. The reason for this is speculated to be linked to the relative energy of the first and the second POD modes. In order to investigate this, the ratio of the eigenvalues normalized by the first mode eigenvalue are presented in Fig. 18. The results in the figure are extracted from Figs. 4(a) and 12(a). Specifically, the result pertaining to the flame front position and the velocity data are shown by the dashed and dotted-dashed curves, respectively. Schematics of the normalized first and the second temporal coefficients distributions pertaining to the flame front position and the velocity data are presented in Figs. 18(b) and 18(c), respectively. These figures mimic the distributions previously presented in Figs. 17(c) and 7(c). The results in Fig. 18 suggest that increasing the ratio of the second to the first eigenvalue transitions the distribution of the first and the second temporal coefficients from a distribution populated at the origin to that populated around a unity radius circle centered at the origin. The circular distribution of the first and second temporal coefficients was discussed to be linked to the transient characteristic of the von Kármán vortex street. In order to further investigate the underlying reason associated with the difference between the distributions in Figs. 18(b) and 18(c), flame front signals with sinusoidal fluctuations were produced. Specifically, 1000 signals were generated with a wavelength of fluctuations identical to that of Flame E condition and with random phase difference between the signals. Then, corresponding normalized eigenvalues

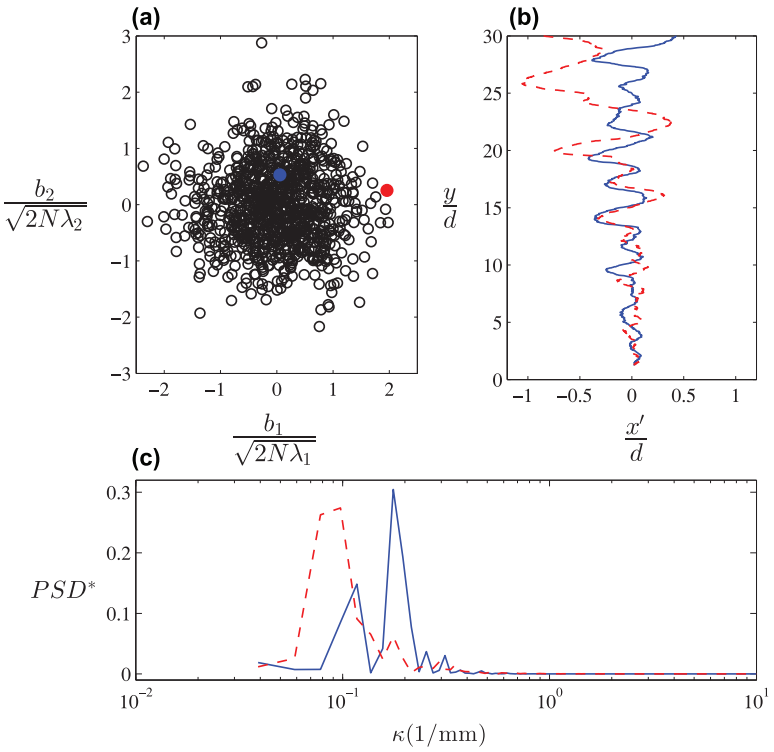

Fig. 17. (a) Variation of the normalized second POD coefficient versus the first POD coefficient associated with Flame E condition. (b) Fluctuations of the flame front position signal along the vertical axis. The blue solid curve pertains to the highlighted data point positioned close to the origin in (a). The red dashed curve corresponds to the data point positioned at a relatively large distance from the origin in (a). (c) Normalized power spectrum densities pertaining to the results presented in (b).

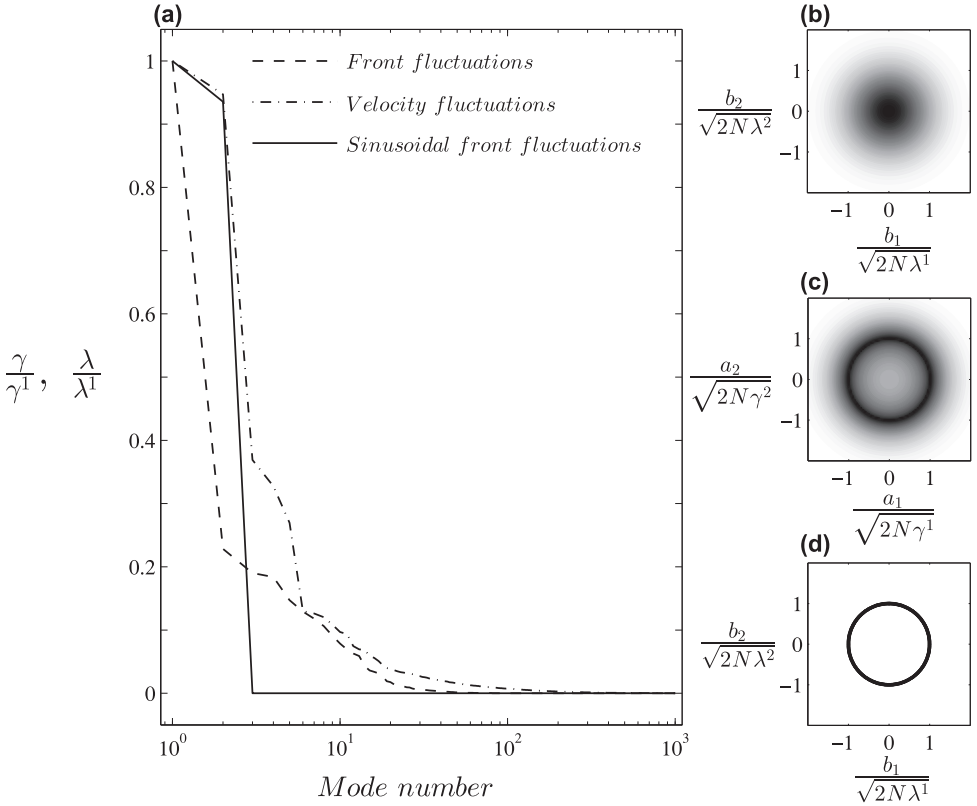

Fig. 18. (a) Normalized eigenvalues of the flame front position signal and the velocity data. The results pertain to Flame E condition. Also presented in the figure is the normalized eigenvalue of sinusoidal flame front fluctuations. (b), (c), and (d) are schematics of the normalized temporal coefficient distributions associated with flame front fluctuations, velocity data, and sinusoidal flame front fluctuations, respectively.

were estimated and the results were presented by the solid line in Fig. 18(a). The corresponding normalized temporal coefficients were obtained and presented in Fig. 18(c). As can be seen from the results in the figure, for sinusoidal fluctuations, the ratio of the second to the first eigenvalues is close to unity and the normalized second and first temporal coefficients are positioned at a unity radius circle. This confirms the conclusion made earlier. That is decreasing λ^2/λ^1 transitions the distribution of the normalized first and second temporal coefficients from a unity radius circle to a distribution which is substantially populated close to the origin.

4. Concluding remarks

Underlying reasons associated with periodicity in corrugations of weakly turbulent premixed V-shaped flames were investigated experimentally. The experiments were conducted using the Mie scattering as well as the Particle Image Velocimetry techniques. All experiments were performed for relatively small value of background turbulence intensity, i.e., $u_{RMS}/U \approx 0.02$. Three Reynolds numbers of 510, 790, and 1057 along with two fuel–air equivalence ratios of 0.6 and 0.7 were tested in the experiments.

In the present investigation, the Proper Orthogonal Decomposition (POD) technique was utilized for analysis of the flame front corrugations. The arguments demonstrate how the POD technique, which is commonly utilized for analysis of non-reacting flows, can be used as a framework for studying turbulent premixed flames.

The results show that the flame fronts are symmetric with respect to the vertical axis and are periodically corrugated in the space domain. Using the vorticity transport equation, the underlying reason associated with the former observation was argued to be linked to the vorticity being an odd function. The characteristics of periodicity in corrugations of the flame fronts were studied using the POD technique. The POD analysis show that the velocity data feature a dominant instability, with corresponding normalized wave number being approximately equal to the Strouhal number 0.22. Analysis of the results pertaining to fluctuations of the flame front position show that relatively large number of the corresponding POD modes are dominated by an instability, with the pertaining wave number being similar to that associated with the velocity data. This suggests the length scale of the flame front fluctuations is dictated by characteristics of non-reacting flow over a circular cylinder.

Although comparison of the length scales associated with non-reacting flow over a circular cylinder and flame front corrugations feature similar trends, the pertaining POD temporal coefficients are significantly different. Specifically, for the flame front position data, the results show that the normalized coefficients are mainly positioned close to the origin; whereas, those associated with the velocity data are positioned around a unity radius circle centered at the origin. The underlying reason was argued to be linked to the ratio of the second and first pertaining eigenvalues. Specifically, it was argued that increasing this ratio causes the energy of the corresponding signal to become distributed mainly between the first and the second POD modes, leading to distribution of the first and the second temporal coefficients around a circle.

Acknowledgments

The authors are grateful for financial support from the Natural Sciences and Engineering Research Council (NSERC) of Canada through discovery (251116-2012) and strategic project (STPGP 430362-12) grants as well as the Ontario Graduate Scholarship (OGS) program.

Appendix A. Convergence analysis

It is discussed in Section 3.1 that the POD technique can be utilized for analysis of the processes that are statistically stationary. This means that the mean of the fluctuations of the corresponding data requires to converge to zero for the time period of investigations. In order to study this, the convergence test was performed for the flame front position, streamwise velocity, and transverse velocity fluctuations, with the corresponding results presented in Figs. 19(a)–19(c), respectively. The results in the Fig. 19(a) are associated with Flame E condition, and those in Figs. 19(b) and 19(c) are associated with the corresponding velocity data for the non-reacting flow condition. The result in Figs. 19(b) and 19(c) are associated with $y/d = 2$ as this vertical distance pertains to the

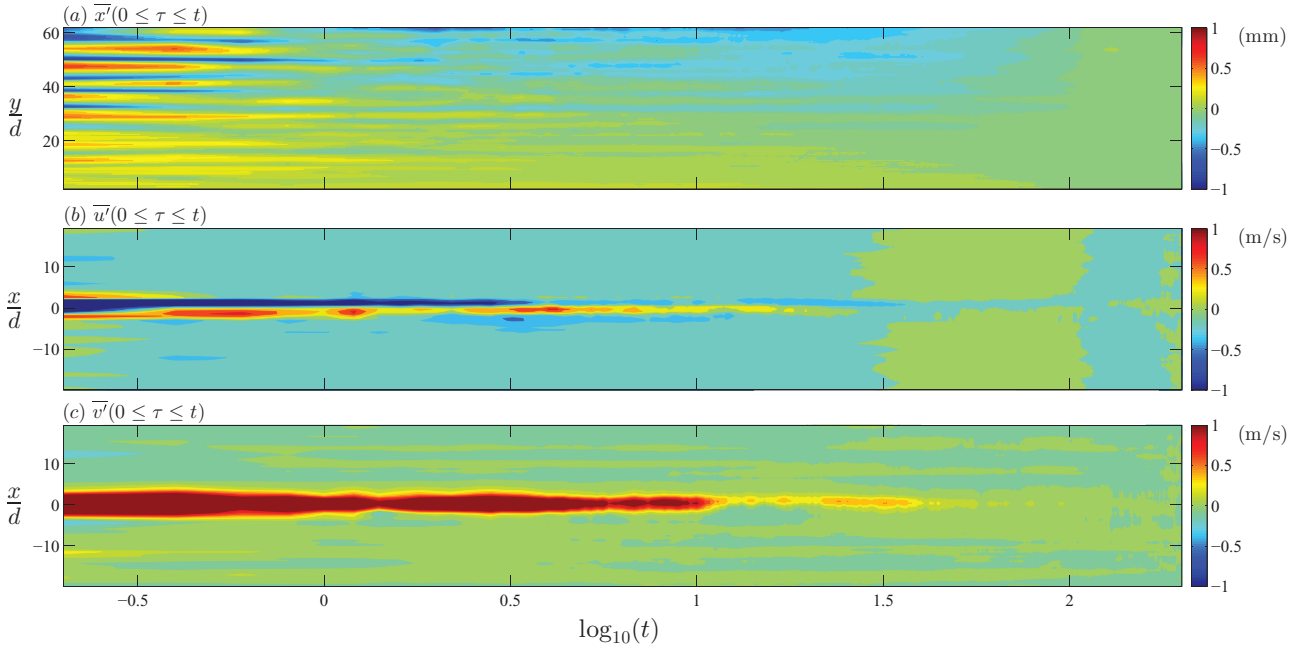

Fig. 19. (a), (b), and (c) are the convergence histories associated with the flame front fluctuations, the streamwise velocity, and the transverse velocity data, respectively.

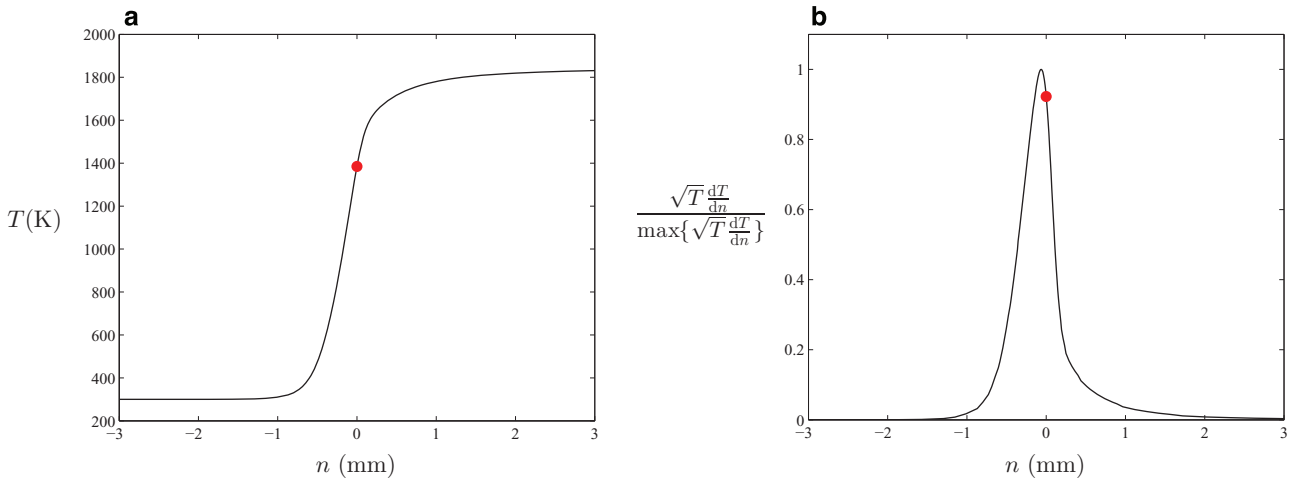

Fig. 20. (a) Temperature variation across an unstretched laminar premixed methane–air flame, with a fuel–air equivalence ratio of 0.7. The results are extracted from the Cantera package. (b) Variation of $\sqrt{T}\mathrm{d}T/\mathrm{d}n$ normalized by the corresponding maximum value. This parameter is related to the velocity change due to thermophoretic force across the flame region.

locations with maximum of velocity fluctuations. The results in Fig. 19 show that the fluctuations of the flame front position, the streamwise, and the transverse velocity data converge to zero. In fact, similar results were obtained for all experimental conditions tested, suggesting that the POD technique can be utilized for the analysis of the flame front position and the velocity data investigated in the present study.

Appendix B. Velocity measurements in the flame region

The POD analysis of the velocity data associated with reacting condition can potentially allow to gain insight into underlying reasons related to symmetric flame front corrugations. However, due to the thermophoretic force being relatively significant over the region associated with possible flame/flow interaction, estimation of the velocity data near the flame region is not feasible for the experimental conditions tested. As a result, the flow structure in this region cannot be fully resolved. This is further elaborated in the following.

For relatively moderate values of the turbulence intensity, the temperature gradient is relatively large at the premixed flame surfaces, see, for example, Chen et al. [63]. As a result, the thermophoretic force, which is related to the gradient of temperature, is substantially pronounced at the flame region [64,65]. Studies of [64,65] show that the thermophoretic force can potentially interfere with the seeding particles following the velocity field fluctuations; and, as a result, can lead to error in the velocity estimation. For spherical seeding particles as well as constant ratio of particles and gas thermal conductivity across the flame region, past studies [64–66] show that the velocity change due to the thermophoretic force is related to the magnitude of the gas temperature gradient normalized by the temperature multiplied by the kinetic viscosity ($\nu|\vec{\nabla}T|/T$). Thus, for an ideal gas as well as a one-dimensional flame configuration, it can be shown that the velocity change due to the thermophoretic force is related to $\sqrt{T}\mathrm{d}T/\mathrm{d}n$, with n being the direction normal to the flame front. In order to assess influence of the thermophoretic force on the velocity change, the temperature variation across an unstretched premixed methane–air flame with a fuel–air equivalence ratio of 0.7 was estimated using the Cantera package and the corresponding results are shown in Fig. 20(a). Values of $\sqrt{T}\mathrm{d}T/\mathrm{d}n$ normalized by the corresponding maximum value are shown in Fig. 20(b). Variation of the CH_3 concentration was extracted from the Cantera simulation and the location of the corresponding maximum was set as the flame front location. In both figures, $n = 0$ is associated with the location of the flame front, with corresponding data points highlighted by the red solid circles. The results in Fig. 20(b) suggest that the influence of the thermophoretic force is significantly pronounced over a distance of approximately ± 1 mm near the flame region. This distance is comparable to the size of the flame front corrugations; hence, the size of possible vortices causing the corrugations. Therefore, resolving the velocity data, near the flame region for studying the interaction of the vortices and the flame front is not feasible for the present investigation, as the region of flame/flow interaction is substantially influenced by the thermophoretic force.

References

[1] N. Peters, Turbulent combustion, first, Cambridge University Press, 2000.
[2] I. Glassman, R.A. Yetter, Combustion, fourth, Elsevier Inc., 2008.
[3] P. Clavin, Dynamic behavior of premixed flame fronts in laminar and turbulent flows, Prog. Energy Combust. Sci. 11 (1985) 1–59.
[4] A.N. Lipatnikov, J. Chomiak, Turbulent flame speed and thickness: phenomenology, evaluation, and application in multi-dimensional simulations, Prog. Energy Combust. Sci. 28 (2002) 1–74.
[5] J.F. Driscoll, Turbulent premixed combustion: Flamelet structure and its effect on turbulent burning velocities, Prog. Energy Combust. Sci. 34 (2008) 91–134.
[6] R.K. Cheng, T.T. Ng, On defining the turbulent burning velocity in premixed V-shaped turbulent flames, Combust. Flame 57 (1984) 155–167.
[7] P. Goix, P. Paranthoen, M. Trinite, A tomographic study of measurements in a V-shaped H_2-air flame and a Lagrangian interpretation of the turbulent flame brush evolution, Combust. Flame 81 (1990) 229–241.
[8] S. Kheirkhah, Ö.L. Gülder, Topology and brush thickness of turbulent premixed V-shaped flames, Flow, Turbul. Combust. 93 (2014) 439–459.
[9] S.J. Shanbhogue, Dynamics of perturbed exothermic bluff-body flow-fields, Georgia Institute of Technology, Atlanta, GA, 2008. Ph.D. thesis.
[10] R.E. Petersen, H.W. Emmons, Stability of laminar flames, Phys. Fluids 4 (1961) 456.
[11] E. Berger, R. Wille, Periodic flow phenomena, Annu. Rev. Fluid Mech. 11 (1972) 313–340.
[12] P.W. Bearman, Vortex shedding from oscillating bluff bodies, Annu. Rev. Fluid Mech. 16 (1984) 195–222.
[13] H. Choi, W. Jeon, J. Kim, Control of flow over a bluff body, Annu. Rev. Fluid Mech. 40 (2008) 113–139.
[14] C.H.K. Williamson, Vortex dynamics in the cylinder wake, Annu. Rev. Fluid Mech. 28 (1996) 477–539.
[15] M.M. Zdravkovich, Flow around circular cylinders: fundamentals, vol. 1, Oxford University Press, 1997.
[16] C. Norberg, Fluctuating lift on a circular cylinder: review and new measurements, J. Fluids Struct. 17 (2003) 57–96.
[17] J.H. Gerrard, The wakes of cylindrical bluff bodies at low Reynolds number, Philos. Trans. R. Soc. Lond. Ser. A, Math. Phys. Sci. 288 (1978) 351–382.
[18] A. Roshko, Experiments on the flow past a circular cylinder at very high Reynolds number, J. Fluid Mech. 10 (1961) 345–356.
[19] P.W. Bearman, On vortex shedding from a circular cylinder in the critical Reynolds number regime, J. Fluid Mech. 37 (1969) 577–585.

[20] C.M. Coat, Coherent structures in combustion, Prog. Energy Combust. Sci. 22 (1996) 427–509.
[21] S.J. Shanbhogue, S. Husain, T. Lieuwen, Lean blowoff of bluff body stabilized flames: Scaling and dynamics, Prog. Energy Combust. Sci. 35 (2009) 98–120.
[22] R.R. Erickson, M.C. Soteriou, P.G. Mehta, The influence of temperature ratio on the dynamics of bluff body stabilized flames, 44th AIAA Aerospace Sciences Meeting and Exhibit (2006). paper 753.
[23] S.M. Bush, E.J. Gutmark, Reacting and non-reacting flow fields of a V-gutter stabilized flame, AIAA J. 45 (2007) 662–672.
[24] J.R. Hertzberg, I.G. Shepherd, L. Talbot, Vortex shedding behind rod stabilized flames, Combust. Flame 86 (1991) 1–11.
[25] S. Yamaguchi, N. Ohiwa, T. Hasegawa, Structure and blow-off mechanism of rod-stabilized premixed flame, Combust. Flame 62 (1985) 31–41.
[26] J.R.G. Bill, K. Tarabanis, The effect of premixed combustion on the recirculation zone of circular cylinders, Combust. Sci. Technol. 47 (1986) 39–53.
[27] C.N. Cross, Combustion heat release effects on asymmetric vortex shedding from bluff bodies, Georgia Institute of Technology, Atlanta, GA, 2011. Ph.D. thesis.
[28] C. Smith, D. Nickolaus, T. Leach, B. Kiel, K. Garwick, LES blowout analysis of premixed flow past V-gutter flameholder, 45th AIAA Aerospace Sciences Meeting and Exhibit (2007). paper 170.
[29] J.L. Lumley, Stochastic tools in turbulence, Academic Press, New York, 1972.
[30] G. Berkooz, P. Holmes, J.L. Lumley, The proper orthogonal decomposition in analysis of turbulent flows, Annu. Rev. Fluid Mech. 25 (1993) 539–575.
[31] K.E. Meyer, P.J. M., O. Özcan, A turbulent jet in cross flow analysed with proper orthogonal decomposition, J. Fluid Mech. 583 (2007) 199–227.
[32] S. Cannon, F. Champagne, A. Glezer, Observations of large-scale structures in wakes behind axisymmetric bodies, Exp. Fluids 14 (1993) 447–450.
[33] J.J. Miau, T.S. Leu, T.W. Liu, J.H. Chou, On vortex shedding behind a circular disk, Exp. Fluids 23 (1997) 225–233.
[34] L. Graftieaux, M. Michard, N. Grosjean, Combining PIV, POD and vortex identification algorithms for the study of unsteady turbulent swirling flows, Meas. Sci. Technol. 12 (2001) 1422–1429.
[35] J.M. Pedersen, K.E. Meyer, POD-analysis of flow structures in a scale model of a ventilated room, Exp. Fluids 33 (2002) 117–149.
[36] S. Bernero, H.E. Fieldler, Application of particle image velocimetry and proper orthogonal decomposition to study of a jet in counterflow, Exp. Fluids 29 (2000) 274–281.
[37] A.C. Eckbreth, Laser diagnostics for combustion temperature and species, second, Overseas Publishers Association, 1996.
[38] J.R. Hertzberg, M. Namazian, L. Talbot, A laser tomographic study of a laminar flame in a Kármán vortex street, Combust. Sci. Technol. 38 (1984) 205–216.
[39] K. Atashkari, M. Lawes, C.G.W. Sheppard, R. Woolley, Towards a general correlation of turbulent premixed flame wrinkling, in: W. Rodi, D. Laurence (Eds.), Proceedings of the 4th International Symposium on EngineeringTurbulence Modelling and Measurements, Engineering Turbulence Modelling and Experiments-4, ISBN 0 08 043328 6 (1999), pp. 805–814.
[40] D.C. Bingham, F.C. Gouldin, D.A. Knaus, Crossed-plane laser tomography: Direct measurement of the flamelet surface normal, Twenty-seventh Symposium (International) on Combustion/The Combustion Institute (1998), pp. 77–84.
[41] J.B. Bell, M.S. Day, I.G. Shepherd, M.R. Johnson, R.K. Cheng, J.F. Grcar, V.E. Beckner, M.J. Lijewski, Numerical simulation of a laboratory-scale turbulent V-flame, Proc. Nat. Acad. Sci. U.S.A. 102 (29) (2005) 10006–10011.
[42] P.C. Miles, F.C. Gouldin, Mean reaction rates and flamelet statistics for reaction rate modelling in premixed turbulent flames, Symp. (Int.) Combust. 24 (1992) 477–484.
[43] D.A. Knaus, F.C. Gouldin, Measurements of flamelet orientations in premixed flames with positive and negative Markstein numbers, Proc. Combust. Inst. 28 (2000) 367–373.
[44] S.S. Sattler, D.A. Knaus, F.C. Gouldin, Determination of three-dimensional flamelet orientation distributions in turbulent V-flames from two-dimensional image data, Proc. Combust. Inst. 29 (2002) 1785–1792.
[45] S. Kheirkhah, Ö.L. Gülder, Turbulent premixed combustion in V-shaped flames: characteristics of flame front, Phys. Fluids 25 (2013) 055107.
[46] N. Peters, Laminar flamelet concepts in turbulent combustion, Symp. (Int.) Combust. 21 (1986) 1231–1250.
[47] G.J. Smallwood, Ö.L. Gülder, D.R. Snelling, B.M. Deschamps, I. Gökalp, Characterization of flame front surfaces in turbulent premixed methane/air combustion, Combust. Flame 101 (1995) 461–470.
[48] Ö.L. Gülder, Contribution of small scale turbulence to burning velocity of flamelets in the thin reaction zone regime, Proc. Combust. Inst. 31 (2007) 1369–1375.
[49] P.C. Miles, Conditional velocity statistics and time-resolved flamelet statistics in premixed turbulent V-shaped flames, Cornell University, Ithaca, NY, 1991 Ph.D. thesis.
[50] T.W. Lee, G.L. North, D.L. Santavicca, Surface properties of turbulent premixed propane/air flames at various Lewis numbers, Combust. Flame 93 (1993) 445–456.
[51] W.L. Roberts, J.F. Driscoll, M.C. Drake, L.P. Goss, Images of quenching of a flame by a vortex-to quantify regimes of turbulent combustion, Combust. Flame 94 (1993) 58–69.
[52] G. Yu, C.K. Law, C.K. Wu, Laminar flame speeds of hydrocarbon + air mixtures with hydrogen addition, Combust. Flame 63 (1986) 339–347.
[53] S.B. Pope, Turbulent flows, Cambridge University Press, 2000.
[54] R. Perrin, M. Braza, E. Cid, S. Cazin, A. Barthet, A. Sevrain, C. Mockett, F. Thiele, Obtaining phase averaged turbulence properties in the near wake of a circular cylinder at high Reynolds number using POD, Exp. Fluids 43 (2007) 341–355.
[55] L. Kourentis, E. Konstantinidis, Uncovering large-scale coherent structures in natural and forced turbulent wakes by combining PIV, POD, and FTLE, Exp. Fluids 52 (2011) 749–763.
[56] B.P. Epps, A.H. Techet, An error threshold criterion for singular value decomposition modes extracted from PIV data, Exp. Fluids 48 (2010) 355–367.
[57] T.K. Sengupta, N. Singh, V.K. Suman, Dynamical system approach to instability of flow past a circular cylinder, J. Fluid Mech. 656 (2010) 82–115.
[58] T. Ruiz, C. Sicot, L.E. Brizzi, J. Borée, Y. Geravis, Pressure/velocity coupling induced by a near wall wake, Exp. Fluids 49 (2010) 147–165.
[59] B.W. van Oudheusden, F. Scarano, N.P. van Hinsberg, D.W. Watt, Phase-resolved characterization of vortex shedding in the near wake of a square-section cylinder at incidence, Exp. Fluids 39 (2005) 86–98.
[60] T.K. Sengupta, S.I. Haider, M.K. Parvathi, G. Pallavi, Enstrophy-based proper orthogonal decomposition for reduced-order modeling of flow past a cylinder, Phys. Rev. E 91 (2015) 043303.
[61] R. Bracewell, The Fourier transform and its applications, McGraw-Hill, New York, 1986.
[62] S.J. Shanbhogue, D.H. Shin, S. Hemchandra, D. Plaks, T. Lieuwen, Flame sheet dynamics of bluff-body stabilized flame during longitudinal acoustic forcing, Proc. Combust. Inst. 32 (2009) 1787–1794.
[63] Y.-C. Chen, N. Peters, G.A. Schneemann, N. Wruck, U. Renz, M.S. Mansour, The detailed flame structure of highly stretched turbulent premixed methane–air flames, Combust. Flame 107 (1996) 223–244.
[64] C.J. Sung, C.K. Law, R.L. Axelbaum, Thermophoretic effects on seeding particles in LDV measurements of flames, Combust. Sci. Technol. 99 (1994) 119–132.
[65] C.J. Sung, J.S. Kistler, M. Nishioka, C.K. Law, Further studies on effects of thermophoresis on seeding particles in LDV measurements of strained flames, Combust. Flame 105 (1996) 189–201.
[66] L. Talbot, R.K. Cheng, R.W. Schefer, D.R. Willis, Thermophoresis of particles in a heated boundary layer, J. Fluid Mech. 101 (1980) 737–758.